Received: Added at production | Revised: Added at production | Accepted: Added at production

DOI: xxx/xxxx

ARTICLE TYPE

Microlayer Model: A nonlinear finite strain viscoelastoplastic formulation for asphalt

Marcel May[1] | Jakob Platen[1] | Erik Kamratowsky[2] | Gustavo Canon Falla[2] | Ines Wollny[1] | Alexander Zeißler[2] | Michael Kaliske[1]

[1]Institute for Structural Analysis, Technische Universität Dresden, 01062 Dresden, Germany

[2]Institute of Urban and Pavement Engineering, Technische Universität Dresden, 01062 Dresden, Germany

Summary

The microlayer framework is an innovative and powerful approach for the numerical simulation of heterogeneous materials, such as aggregate-matrix composites across multiple scales. In this study, the microlayer framework is extended for the first time to account for viscoelastic-elastoplastic material behavior. The kinematics of the representative volume element (RVE) at the microscale are designed to accurately capture the behavior of typical composites, such as asphalt or concrete. The constitutive equations at the microscale are developed independently of the macroscale, ensuring the necessary conditions for proper computational homogenization. The thermodynamically motivated scale transition is carried out using the Principle of Multiscale Virtual Power (PMVP). In numerical studies, it is shown by embedding classical material models at the micro level that homogenization leads to physically meaningful triaxial, mechanical behavior at the macro level. It is demonstrated that with a suitable choice of microlayer geometry, the tensile-compressive anomaly of the stress-strain behavior observed in aggregate-matrix composites can be modeled without modifying the material model. Finally, the quality of the microlayer framework is shown by validating a triaxial test of an asphalt specimen with a complex cyclic harmonic axial and radial loading regime.

KEYWORDS:
Microlayer framework, Finite strain viscoelasticity, stress-free intermediate configuration

1 | INTRODUCTION

Heterogeneos materials are present in many engineering applications. Within numerical simulations e.g. using the finite element method (FEM), a smeared (or homogenized) analysis of such materials can only be performed using phenomenological models that represent the macroscopically observed material properties. To capture the actual physical effects or mechanisms arising from the composite's microstructural composition, other approaches such as multiscale analyses must be employed. Particularly noteworthy in this context is the asymmetry of the stiffness between the tensile and compression areas, e.g. in case of asphalt, which is a mixture of aggregates, bituminous binder and additives, where the stiffness at compression load is higher due to the interlocking of the aggregates (additional load transmission from aggregate to aggregate) while at tension load this interlocking does not take place and the whole load has to be transmitted from binder to aggregate and vice versa. A realistic simulation of asphalt pavements at rolling tire load requires among others the consideration of the different material behavior at

compression and tension, since in pavements complex three-dimensional combined compression-tension stress states arise due to the bending behavior of the structure[1,2]. Classical multiscale approaches, where the finite element problem has to be solved on each scale, are computationally too expensive for large-scale road structures, especially with regard to the consideration of the occurring finite strains in the constitutive formulation[3]. Therefore, in this work, the microscale is modeled with basic 3D geometric shapes inspired by the real asphalt structure in order to solve the microscale problem analytically[4]. The microlayer framework can therefore be considered as an advancement of the well-documented microplane model[5,6,7], which was originally developed for concrete. In these works, a unit sphere is introduced at each material point of the macroscale. The surface of this sphere is discretized by planes to enable numerical integration. By projecting specific components of the macroscopic strain tensor onto each plane, a set of vectorial strain measures is defined on each plane, which are then converted into vectorial stress measures using constitutive equations. The macroscopic stress tensor of the microplane model is subsequently formed by homogenizing the stress components across all orientations. However, both the projection and the subsequent homogenization are not physically sound. For the projection and splits, such as the V-D split or the N-T split[8], the macroscopic strain tensor is required. Consequently, the material law at the micro level is inherently influenced by the one of the macro level, which inverts classical multiscale analysis theory[9]. The homogenization of the conjugated stresses is, thus, also simplified and therefore not thermodynamically motivated[10]. If finite strains of the matrix are expected under load[11], e.g. in asphalt in case of rutting, the microplane concept would fail. By visualizing the matrix as a plane surface, the tensorial character of the strain tensor is lost. To overcome this drawback, the microlayer framework is used in this work[4,10]. While previous microlayer models are restricted to elastoplastic[4] or viscoelastic[12] behavior, the microlayer framework is extended in this study to viscoelastic-elastoplastic behavior for the first time. Within the microlayer framework, the aggregates are still modeled as infinitely stiff components. However, instead of using planes to describe the constitutive laws, polyhedrons are introduced which are imprinted on the surfaces of the discretized unit sphere. Due to the three-dimensional geometry of these layers, it is feasible to employ established material laws that incorporate complete second-order stress and strain tensors. The introduction of triaxially deformable layers also means that the development of the mechanical response of all scales is determined by the kinematics of the microscale. Due to the strict separation, multiplicative splits of the deformation gradient are also thermodynamically meaningful. Finally, only the introduction of three-dimensional kinematics allows the application of the thermodynamically motivated *Principle of Multiscale Virtual Power* (PMVP)[9] for the scale transition. Using well-established classical models for elastoplasticity and viscoelasticity at finite strains, numerical examples demonstrate that material properties are preserved during homogenization. Furthermore, it is shown that the geometrical structure of the microscale can be utilized to represent anisotropic mechanical properties at the macroscale. It is shown for the first time that, through an appropriate choice of the ratio between microlayer thickness and aggregate radius, the typical asymmetry between tensile and compressive behavior in composites can be specifically controlled. The application of the microlayer model to represent a triaxial test of an asphalt specimen demonstrates its capability to be used for realisic simulations.

2 | MICROLAYER FRAMEWORK

2.1 | Deformation gradient and strain energy function

In continuum mechanics, a solid body $\mathcal{B}$ occupies a region in the Euclidean space $\mathbb{R}^3$. At the initial time $t = 0$, the body is in its reference configuration $\mathcal{B}_0$, which is assumed to be stress-free. As time progresses ($t > 0$), the body deforms and takes on a new shape, denoted as $\mathcal{B}_t$[13]. In this contribution, the classical Cauchy-Boltzmann continuum assumption is adopted, i.e., interactions are local and the stress response depends only on the first deformation gradient (equivalently, on the displacement gradient). The motion of the body is described by the mapping

$$\boldsymbol{\varphi}_t : \mathcal{B}_0 \to \mathcal{B}_t, \quad \boldsymbol{X} \mapsto \boldsymbol{x}, \tag{1}$$

where $\boldsymbol{X}$ represents the initial position of a material point in $\mathcal{B}_0$ (material), and $\boldsymbol{x}$ is its current position in $\mathcal{B}_t$ (spatial). To characterize local deformations, the deformation gradient is introduced

$$\boldsymbol{F} = \frac{\partial \boldsymbol{\varphi}_t}{\partial \boldsymbol{X}}. \tag{2}$$

This tensor describes how line elements of the body change length and orientation. The displacement field is given by

$$\boldsymbol{u}(\boldsymbol{X}, t) = \boldsymbol{x} - \boldsymbol{X}, \tag{3}$$

which measures the change in position of each material point. The deformation gradient can, therefore, also be expressed as a function of the displacement gradient

$$\boldsymbol{F} := \frac{\partial \boldsymbol{\varphi}_t}{\partial \boldsymbol{X}} = \mathrm{Grad}(\boldsymbol{\varphi}_t) = \mathrm{Grad}(\boldsymbol{u}) + \boldsymbol{I} = \boldsymbol{H} + \boldsymbol{I}, \tag{4}$$

where $\boldsymbol{I}$ is the second order identity tensor. This decomposition captures both rigid body motion and deformation effects such as stretching and shearing. The displacement gradient $\mathrm{Grad}(\boldsymbol{u})$ is identified with $\boldsymbol{H}$. To describe the energy stored in $\mathcal{B}$, the Helmholtz free energy ψ has to be derived from the Gibbs equation via a partial Legendre transformation [14]. Within the general phenomenological approach, assuming that only mechanical deformations induce stresses, ψ depends on the deformation gradient $\boldsymbol{F}$ and some internal variables

$$\psi = \psi(\boldsymbol{F}). \tag{5}$$

For the scale transition to the macro level of the microlayer model presented in this paper, the first Piola-Kirchhoff stress tensor can be used as the stress quantity conjugate to $\boldsymbol{F}$

$$\boldsymbol{P} = \frac{\partial \psi}{\partial \boldsymbol{F}}. \tag{6}$$

$\boldsymbol{P}$ connects forces in the current configuration to areas in the reference configuration. The corresponding material tangent is then given by

$$\mathbb{C}^{\boldsymbol{P}} = \frac{\partial \boldsymbol{P}}{\partial \boldsymbol{F}}. \tag{7}$$

2.2 | Multiscale analysis

The macroscopic behavior of engineering materials, such as asphalt, is strongly influenced by their microstructural features [15]. Multiscale analysis provides a framework to transfer the effects of the microscale to the macroscale, enabling a more accurate representation of material behavior [9,16]. The concept of scale separation is fundamental to multiscale analysis and is based on the assumption that the characteristic length of the microscale is significantly smaller than the characteristic length of the macroscale. A common criterion for this separation is that the ratio should be at least ten. This condition is typically met in large-scale asphalt experiments, such as triaxial or cyclic indirect tensile tests, as well as in the typical thicknesses of asphalt layers in road pavements. The microstructure can then be described using a representative volume element (RVE). An RVE is a portion of the microscale. Its volume must be large enough to represent the mechanical behavior of the microscale, but small enough to reduce the computational effort, as the effort is directly dependent on the number of degrees of freedom on the microscale. In this work, the coupling between RVE and a material point of the macroscale is defined by means of the themodynamically motivated *Principle of Multiscale Virtual Power* (PMVP) [9]. The PMVP is a unified variational approach, which is an extension of the classic Hill-Mandel principle [17]. In addition to the balance of internal virtual power, the external virtual power at the point $\boldsymbol{X}^{\mathcal{M}}$ of the macroscale is also included in the balance of the total power of the RVE. The core idea of the multiscale approach is to map the macroscopic quantities $\square^{\mathcal{M}}$ for each material point to the corresponding microscopic fields $\square^{m}$ by means of a linear *insertion operator* (macro → micro). The reverse scale transition (micro → macro) is performed by *homogenization operators*, which are linear in all arguments. Both links must be chosen such that the magnitude of the relevant kinematical quantities is preserved across the scale transition. This postulate is referred to as the *Principle of Kinematical Admissibility*. First, the kinematics on both scales are specified. On the macroscale, this work restricts the set of generalized displacements to the displacement field of points $\boldsymbol{X}^{\mathcal{M}}$

$$\boldsymbol{u}^{\mathcal{M}} = \boldsymbol{u}^{\mathcal{M}}(\boldsymbol{X}^{\mathcal{M}}), \tag{8}$$

(cf. Equation (3)). As generalized strain–action operator, the linear reference gradient is chosen, hence the generalized strain is the displacement gradient

$$\boldsymbol{H}^{\mathcal{M}} = \mathrm{Grad}(\boldsymbol{u}^{\mathcal{M}}), \tag{9}$$

(cf. Equation (4)). Other multiphysical definitions are possible. We only take the first derivative of the displacements, which is reasonable for Cauchy-Boltzmann continua. For higher order continua more derivatives should be taken into account. However, the focus of this contribution is on classical finite-strain solid mechanics. Analogously, the microscopic kinematical fields within the RVE are defined as

$$\boldsymbol{u}^{m} = \boldsymbol{u}^{m}(\boldsymbol{X}^{m}), \tag{10}$$

$$\boldsymbol{H}^{m} = \mathrm{Grad}(\boldsymbol{u}^{m}), \tag{11}$$

where $\boldsymbol{X}^m$ denotes microscopic reference coordinates. Without loss of generality, the microscopic displacement is additively split into a part that depends on the macroscopic point $\boldsymbol{X}^{\mathcal{M}}$ and a local fluctuation

$$\boldsymbol{u}^m(\boldsymbol{X}^m) = \overline{\boldsymbol{u}}^m\left(\boldsymbol{X}^{\mathcal{M}};\, \boldsymbol{X}^m\right) + \tilde{\boldsymbol{u}}^m(\boldsymbol{X}^m), \tag{12}$$

where the field $\overline{\boldsymbol{u}}^m(\boldsymbol{X}^{\mathcal{M}}; \boldsymbol{X}^m)$ denotes the macro-point–dependent contribution and $\tilde{\boldsymbol{u}}^m(\boldsymbol{X}^m)$ represents the microscopic fluctuation. To connect the scales, the insertion operators map the macroscopic kinematical quantities at a given macroscopic point $\boldsymbol{X}^{\mathcal{M}}$ to the corresponding microscopic fields defined over the RVE domain Ω. These operators embed the macroscopic state into the microscale in a kinematically admissible way, ensuring compatibility between both descriptions. Two linear insertion operators are introduced: $\boldsymbol{J}_U^m$, which maps the macroscopic generalized displacements to the microscopic displacement space, and $\boldsymbol{J}_E^m$, which maps the macroscopic generalized strains to the microscopic strain–action space. They act on the generalized displacements and strains, respectively. Applied to the macroscopic quantities $\boldsymbol{u}^{\mathcal{M}}$ and $\boldsymbol{H}^{\mathcal{M}}$, the resulting microscopic fields are expressed as

$$\overline{\boldsymbol{u}}^m = \boldsymbol{J}_U^m\left(\boldsymbol{u}^{\mathcal{M}}\right) \;+\; \boldsymbol{J}_E^m\left(\boldsymbol{H}^{\mathcal{M}}\right), \tag{13}$$

representing the macro-induced part of the microscopic displacement introduced in Equation (12). For Cauchy-Boltzmann continua within the framework of finite-strain solid mechanics, the classical choice for these operators is a linear mapping of the macroscopic displacement and displacement gradient onto the microscopic coordinates

$$\overline{\boldsymbol{u}}^m(\boldsymbol{X}^{\mathcal{M}}; \boldsymbol{X}^m) = \boldsymbol{u}^{\mathcal{M}}(\boldsymbol{X}^{\mathcal{M}}) + \boldsymbol{H}^{\mathcal{M}}(\boldsymbol{X}^{\mathcal{M}})\left(\boldsymbol{X}^m - \boldsymbol{X}_0^m\right), \tag{14}$$

under the modeling assumption that the microscale coordinates are referenced to the RVE centroid,

$$\boldsymbol{X}_0^m = \frac{1}{V}\int_{\Omega} \boldsymbol{X}^m \,\mathrm{d}V. \tag{15}$$

This choice ensures objectivity and invariance with respect to rigid translations of the RVE. Equation (14) thus corresponds to a first-order (affine) insertion of the macroscopic deformation into the microscale. More complex definitions of the insertion operators are possible (e.g., including higher-order gradients, nonlocal dependencies, or additional multiphysical fields), but the present contribution focuses on the classical case of finite-strain solid mechanics. Having specified the macro-induced part of the microscopic fields via the insertion operators, the reverse linkage from micro to macro is established by introducing homogenization operators that extract the effective macroscopic kinematics from the microscopic fields under the adopted fluctuation constraints. Two linear homogenization operators are introduced: H_U^m, which maps the microscopic displacement field space to the point-valued macroscopic generalized displacement space, and H_E^m, which maps the microscopic strain–action field space to the point-valued macroscopic generalized strain space. Applied to the microscopic displacement and displacement-gradient fields, these operators provide the homogenized macroscopic quantities as

$$\boldsymbol{u}^{\mathcal{M}} = H_U^m\left[\boldsymbol{u}^m\right], \qquad \boldsymbol{H}^{\mathcal{M}} = H_E^m\left[\boldsymbol{H}^m\right]. \tag{16}$$

Correspondingly, the fluctuation fields satisfy the kernel (zero-mean) conditions

$$H_U^m\left[\tilde{\boldsymbol{u}}^m\right] = \boldsymbol{0}, \qquad H_E^m\left[\tilde{\boldsymbol{H}}^m\right] = \boldsymbol{0}, \tag{17}$$

which, for the specific choice of volume-averaging operators, reduce to

$$\int_{\Omega} \tilde{\boldsymbol{u}}^m \,\mathrm{d}V = \boldsymbol{0}, \qquad \int_{\Omega} \tilde{\boldsymbol{H}}^m \,\mathrm{d}V = \boldsymbol{0}. \tag{18}$$

These conditions stem from kinematical admissibility, "insertion followed by homogenization" reproduces the prescribed macroscopic state, and imply that fluctuations lie in the kernels of the homogenization operators, so macroscopic quantities depend only on the macro-induced part of the microscopic fields. In the present contribution, the concrete realization of the homogenizers is assumed to be simple (unit-weighted) volume averaging over the RVE. This modeling choice is standard in classical multiscale approaches because it is objective (with centroidal referencing), acts as a left inverse to the first-order (affine) insertion, and avoids spurious dependence on the RVE's position or shape beyond its volume. Accordingly, the macroscopic displacement and displacement gradient are defined by

$$\boldsymbol{u}^{\mathcal{M}} \;=\; \frac{1}{V}\int_{\Omega} \boldsymbol{u}^m \,\mathrm{d}V, \qquad \boldsymbol{H}^{\mathcal{M}} \;=\; \frac{1}{V}\int_{\Omega} \boldsymbol{H}^m \,\mathrm{d}V, \tag{19}$$

which, together with the zero-mean fluctuation conditions, enforce a unique macro–micro split and kinematical consistency of the scale transition. Moreover, the zero-mean constraint for the microscopic gradient of the fluctuation admits the equivalent boundary form

$$\int_{\Omega} \tilde{\boldsymbol{H}}^m \, \mathrm{d}V \;=\; \int_{\partial\Omega} \boldsymbol{N}^m \otimes \tilde{\boldsymbol{u}}^m \, \mathrm{d}A \;=\; \boldsymbol{0}, \tag{20}$$

obtained by the divergence theorem. $\boldsymbol{N}^m$ denotes the unit outward normal in the reference configuration. Therefore, the space of kinematically admissible fluctuation displacements at microscale is

$$\mathcal{K}^m := \left\{ \boldsymbol{u}^m \in V \;\middle|\; \int_{\partial\Omega} \boldsymbol{N}^m \otimes \boldsymbol{u}^m \, \mathrm{d}A = \boldsymbol{0} \;;\; \int_{\Omega} \boldsymbol{u}^m \, \mathrm{d}V = \boldsymbol{0} \right\}, \tag{21}$$

and the fluctuation field is required to satisfy

$$\tilde{\boldsymbol{u}}^m \in \mathcal{K}^m. \tag{22}$$

Based on mechanical considerations, $\mathcal{K}^m$ will be further specialized in the next section, and a concrete RVE for aggregate-matrix composites is introduced. The second fundamental postulate of the multiscale framework is the *mathematical duality* between the introduced kinematical quantities and their corresponding stress- or force-like counterparts. This duality ensures that each kinematic variable has a unique energetic conjugate, such that their product represents a power term contributing to the virtual power balance. Following this principle, the macroscopic displacement gradient $\boldsymbol{H}^{\mathcal{M}}$ is energetically conjugate to the macroscopic first Piola–Kirchhoff stress tensor $\boldsymbol{P}^{\mathcal{M}}$, and the macroscopic displacement $\boldsymbol{u}^{\mathcal{M}}$ is conjugate to the macroscopic body force $\boldsymbol{b}^{\mathcal{M}}$. Analogously, on the microscale, the microscopic counterparts $\boldsymbol{H}^m$, $\boldsymbol{u}^m$, $\boldsymbol{P}^m$, and $\boldsymbol{b}^m$ form the corresponding dual pairs. The PMVP used here is a specialization of Blanco's general multiscale power statement[9] to these choices. In essence, the PMVP states that the virtual power of internal and external actions must be identical when computed on the macroscale and on the microscale. This leads directly to the generalized Hill–Mandel condition

$$V\, \boldsymbol{P}^{\mathcal{M}} : \delta\dot{\boldsymbol{H}}^{\mathcal{M}} - V\, \boldsymbol{b}^{\mathcal{M}} \cdot \delta\dot{\boldsymbol{u}}^{\mathcal{M}} \overset{!}{=} \int_{\Omega} \boldsymbol{P}^m : \delta\dot{\boldsymbol{H}}^m \, \mathrm{d}V - \int_{\Omega} \boldsymbol{b}^m \cdot \delta\dot{\boldsymbol{u}}^m \, \mathrm{d}V, \tag{23}$$

which enforces the equality of virtual powers on both scales and thus guarantees energetic consistency between micro and macro kinematics. This equality is not a postulated averaging rule but follows from the kinematical admissibility of the insertion and homogenization operators together with the zero-mean fluctuation constraints introduced earlier. By isolating the terms associated with the admissible macroscopic variations $\delta\dot{\boldsymbol{H}}^{\mathcal{M}}$ and $\delta\dot{\boldsymbol{u}}^{\mathcal{M}}$ in Equation (23), the corresponding macroscopic stress and body force densities emerge naturally as weighted averages of their microscopic counterparts

$$\boldsymbol{P}^{\mathcal{M}} = \frac{1}{V} \int_{\Omega} \left[\boldsymbol{P}^m - (\boldsymbol{X}^m - \boldsymbol{X}_0^m) \otimes \boldsymbol{b}^m \right] \mathrm{d}V, \tag{24}$$

$$\boldsymbol{b}^{\mathcal{M}} = \frac{1}{V} \int_{\Omega} \boldsymbol{b}^m \, \mathrm{d}V. \tag{25}$$

The first term in Equation (24) represents the volumetric contribution of the microscopic stresses, while the second term accounts for the moment of the microscopic body forces with respect to the centroidal reference position $\boldsymbol{X}_0^m$. This correction ensures that the macroscopic stress is invariant under rigid translations of the RVE, preserving objectivity and guaranteeing that both force and moment equilibria are satisfied at the macroscale[4,10,12,18].

2.3 | Microlayer formulation

The aim of this section is to provide an appropriate RVE for the modeling of aggregate-matrix composites. In contrast to computationally intensive FE^2 approaches, where all scales are modeled and discretized as sections of actual material geometries, an analytical solution of the material problem is used in this contribution. Inspired by the micro-structural assumptions of the well known micro-plane model from Bažant[19] and the real mesogeometry of asphalt, the microscale is represented by a infinitely stiff, convex aggregate Ω^k, on whose surface m_{ml} deformable layers Ω^i are imprinted. The domain results in

$$\Omega = \Omega^k \cup \bigcup_{i=1}^{m_{ml}} \Omega^i \tag{26}$$

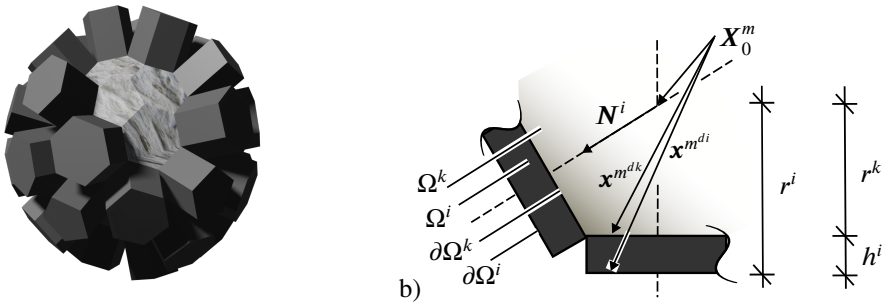

Figure 1 a) Illustration of a feasible shape of the RVE and b) geometry definition.

and is illustrated in Figure 1. The individual RVEs are connected via the layers. It is assumed that the aggregates are deterministically distributed and that their relative displacements generate the macroscopic strains and control the deformation of the adjacent layers. Under the assumption that the aggregates are not interconnected, a homogeneous strain field is obtained in the layers, in analogy to [19].

The distance between the aggregate center and the outer surface $\partial\Omega^i$ of layer i is defined by

$$r^i = r^k + h^i. \tag{27}$$

Here, h^i denotes the thickness of layer i and r^k is the distance from the aggregate center $\boldsymbol{X}_0^m$ to the aggregate surface $\partial\Omega^k$ associated with i. In principle, r^k may be chosen arbitrarily subject to convexity. However, in this contribution it is assumed r^k to be constant for all layers. The vector $\boldsymbol{N}^i$ denotes the unit normal of layer i. The kinematics of the microscale in this contribution follow the basic mechanical models from [4]: No strains can occur at the domain of the aggregate at the microscale. However, macroscopic translational and rotational motions of the aggregate are admissible. It is further assumed that, at the aggregate center $\boldsymbol{X}_0^m$, only macroscopic translations are present. For the aggregate microscale displacementfield $\boldsymbol{u}^m_{\boldsymbol{x}^{m^k}\in\Omega^k}$, with $\boldsymbol{x}^{m^k} \in \Omega^k$, Equation (12) must be satisfied.

Therefore, the displacement field $\boldsymbol{u}^m_{\boldsymbol{x}^{m^k}\in\Omega^k}$ results from the macroscopic translations and rotations $\boldsymbol{R}^{\mathcal{M}}$ (strain-free component of the deformation gradient ($\boldsymbol{R} = \boldsymbol{F}\cdot\boldsymbol{U}^{-1}$)) around the geometric center $\boldsymbol{X}_0^m$ of the aggregate

$$\boldsymbol{u}^m_{\boldsymbol{x}^{m^k}\in\Omega^k} = \boldsymbol{u}^{\mathcal{M}} + \boldsymbol{H}^{\mathcal{M}}\cdot(\boldsymbol{x}^{m^k} - \boldsymbol{X}_0^m) + \underbrace{(\boldsymbol{1} - \boldsymbol{U}^{\mathcal{M}})\cdot(\boldsymbol{x}^{m^k} - \boldsymbol{X}_0^m)}_{\tilde{\boldsymbol{u}}^m_{\boldsymbol{x}^{m^k}\in\Omega^k}}, \tag{28}$$

which leads to

$$\boldsymbol{u}^m_{\boldsymbol{x}^{m^k}\in\Omega^k} = \underbrace{\boldsymbol{u}^{\mathcal{M}}}_{\text{translation}} + \underbrace{(\boldsymbol{R}^{\mathcal{M}} - \boldsymbol{1})\cdot(\boldsymbol{x}^{m^k} - \boldsymbol{X}_0^m)}_{\text{rotation}}. \tag{29}$$

The displacement fluctuations $\tilde{\boldsymbol{u}}^m_{\boldsymbol{x}^{m^k}\in\Omega^k}$ have to offset all deformations from the macroscopic displacement gradient $\boldsymbol{H}^{\mathcal{M}}$. This is possible because the translational displacements fulfill the requirement of Equation (21). Assuming the layers remain flat, which implies that the outer plane $\partial\Omega^i$ is a symmetry plane to the aggregate-layer interface $\partial\Omega^k$, the displacement fluctuations must vanish at $\partial\Omega^i$, therefore with Equation (12) the following applies to the displacements $\boldsymbol{u}^m_{\boldsymbol{x}^{m^{di}}\in\partial\Omega^i}$ at $\partial\Omega^i$

$$\boldsymbol{u}^m_{\boldsymbol{x}^{m^{di}}\in\partial\Omega^i} = \boldsymbol{u}^{\mathcal{M}} + (\boldsymbol{F}^{\mathcal{M}} - \boldsymbol{1})\cdot(\boldsymbol{x}^{m^{di}} - \boldsymbol{X}_0^m). \tag{30}$$

Assuming a homogeneous displacement gradient, the displacement field $\boldsymbol{u}_{\boldsymbol{x}^{m^i}\in\Omega^i}$ between the planes $\partial\Omega^i$ and $\partial\Omega^k$ is linear. Under the additional assumption that no separation between aggregates and layers can occur (so that $\partial\Omega^k$, $\partial\Omega^i \subset \Omega^i$), a linear interpolation between the known displacement fields of the layer Ω^i yields

$$\boldsymbol{u}^m_{\boldsymbol{x}^{m^i}\in\Omega^i} = \boldsymbol{u}^m_{\boldsymbol{x}^{m^{dk}}\in\partial\Omega^k} f(\boldsymbol{x}^{m^i}) + \boldsymbol{u}^m_{\boldsymbol{x}^{m^{di}}\in\partial\Omega^i}[1 - f(\boldsymbol{x}^{m^i})], \tag{31}$$

with

$$f(\boldsymbol{x}^{m^i}) = \frac{r^i}{h^i} - \frac{1}{h^i}(\boldsymbol{x}^{m^i} - \boldsymbol{X}_0^m)\cdot\boldsymbol{N}^i, \tag{32}$$

and

$$\boldsymbol{u}^m_{\boldsymbol{x}^{m^{dk}}\in\partial\Omega^k} = \boldsymbol{u}^{\mathcal{M}} + (\boldsymbol{R}^{\mathcal{M}} - \boldsymbol{1})\cdot(\boldsymbol{x}^{m^{dk}} - \boldsymbol{X}_0^m). \tag{33}$$

However, inserting and rearranging leads to a quadratic dependence on the location $\boldsymbol{x}^{m^i}$ ($\partial\Omega^k$, $\partial\Omega^i \subset \Omega^i$)

$$\boldsymbol{u}^m_{\boldsymbol{x}^{m^i}\in\Omega^i} = \boldsymbol{u}^{\mathcal{M}} + (\boldsymbol{F}^{\mathcal{M}} - \mathbf{1}) \cdot (\boldsymbol{x}^{m^{di}} - \boldsymbol{X}^m_0) + \left[\frac{r^i}{h^i} - \frac{1}{h^i}(\boldsymbol{x}^{m^i} - \boldsymbol{X}^m_0) \cdot \boldsymbol{N}^i\right] \left\{ (\boldsymbol{R}^{\mathcal{M}} - \mathbf{1})(\boldsymbol{x}^{m^{dk}} - \boldsymbol{X}^m_0) - (\boldsymbol{F}^{\mathcal{M}} - \mathbf{1})(\boldsymbol{x}^{m^{di}} - \boldsymbol{X}^m_0) \right\}, \tag{34}$$

which contradicts the requirement of a linear homogeneous displacement gradient. By splitting $\boldsymbol{x}^{m^{di}}$ and $\boldsymbol{x}^{m^{dk}}$ into radial $\boldsymbol{x}^{\square}_r$ and tangential $\boldsymbol{x}^{\square}_t$ components

$$\boldsymbol{x}^{m^{di}} = \boldsymbol{x}^{m^{di}}_r + \boldsymbol{x}^{m^{di}}_t + \boldsymbol{X}^m_0 = \boldsymbol{N}^i r^i + \boldsymbol{x}^{m^{di}}_t + \boldsymbol{X}^m_0 \tag{35}$$

and

$$\boldsymbol{x}^{m^{dk}} = \boldsymbol{x}^{m^{dk}}_r + \boldsymbol{x}^{m^{dk}}_t + \boldsymbol{X}^m_0 = \boldsymbol{N}^i r^k + \boldsymbol{x}^{m^{dk}}_t + \boldsymbol{X}^m_0, \tag{36}$$

according to[4], it is feasible to transform all displacement-determining radial components into linear relations. In order to obtain the homogeneous strain state, the assumption is made that the tangential components $\boldsymbol{x}^{m^{dk}}_t$ and $\boldsymbol{x}^{m^{di}}_t$ of the position vectors on $\partial\Omega^i$ and $\partial\Omega^k$ are negligibly small, which ultimately results in the kinematic coupling operator of the layer displacement

$$\boldsymbol{u}^m_{\boldsymbol{x}^{m^i}\in\Omega^i} = \boldsymbol{u}^{\mathcal{M}} + (\boldsymbol{F}^{\mathcal{M}} - \mathbf{1}) \cdot (\boldsymbol{x}^{m^i} - \boldsymbol{X}^m_0) + \left[\frac{r^i}{h^i} - \frac{1}{h^i}(\boldsymbol{x}^{m^i} - \boldsymbol{X}^m_0) \cdot \boldsymbol{N}^i\right] \left\{ \boldsymbol{R}^{\mathcal{M}} \cdot [\mathbf{1} - \boldsymbol{U}^{\mathcal{M}}] \cdot \boldsymbol{N}^i r^i - \boldsymbol{R}^{\mathcal{M}} \cdot \boldsymbol{N}^i h^i + h^i \boldsymbol{N}^i \right\}. \tag{37}$$

The displacement gradient results in

$$\boldsymbol{H}^{m^i} = \frac{\partial \boldsymbol{u}^m_{\boldsymbol{x}^{m^i}\in\Omega^i}}{\partial \boldsymbol{x}^{m^i}} = -\frac{1}{h^i}\left\{ r^k \left(\frac{\boldsymbol{n}^i}{|\boldsymbol{n}^i|} - \boldsymbol{n}^i \right) + (\boldsymbol{N}^i - \boldsymbol{n}^i) h^i \right\} \otimes \boldsymbol{N}^i. \tag{38}$$

To obtain Equation (38), the abbreviations

$$\boldsymbol{n}^i = \boldsymbol{F}^{\mathcal{M}} \cdot \boldsymbol{N}^i \tag{39}$$

and

$$\frac{\boldsymbol{n}^i}{|\boldsymbol{n}^i|} = \boldsymbol{R}^{\mathcal{M}} \cdot \boldsymbol{N}^i \tag{40}$$

are incorporated. It becomes obvious that the deformation behavior of the microlayer depends on its orientation $\boldsymbol{n}^i$ and thickness h^i. The latter allows viscoelastic and elastoplasctic material behavior to be taken into account within a finite strain theory.

For absent body forces, the stress homogenization operator, which translates the stresses $\boldsymbol{P}^m$ of the RVE to the macroscale $\boldsymbol{P}^{\mathcal{M}}$, is a direct outcome of the kinematic coupling operators and the PMVP

$$V\, \boldsymbol{P}^{\mathcal{M}} : \delta \dot{\boldsymbol{H}}^{\mathcal{M}} \overset{!}{=} \int_{\Omega} \boldsymbol{P}^m : \delta \dot{\boldsymbol{H}}^m dV. \tag{41}$$

The macroscopic stresses result from the volume average of the layer and aggregate stresses

$$\boldsymbol{P}^{\mathcal{M}} = \frac{1}{V}\left[\sum_{i=1}^{m_{ml}} \int_{\Omega^i} \boldsymbol{P}^{m^i} \mathrm{d}V + \int_{\Omega^k} \boldsymbol{P}^{m^k} \mathrm{d}V \right]. \tag{42}$$

In the aggregate region local equilibrium holds, i.e. the balance of linear momentum

$$\operatorname{div} \boldsymbol{P}^{m^k} = \mathbf{0}. \tag{43}$$

Applying the product rule to $r_j = x^m_j - X^m_{0j}$ gives

$$\left[P^{m^k}_{\ell k} r_j\right]_{,k} = P^{m^k}_{\ell k,k}\, r_j + P^{m^k}_{\ell j}. \tag{44}$$

Since $P^{m^k}_{\ell k,k} = 0$, this simplifies to

$$P^{m^k}_{\ell j} = \left[P^{m^k}_{\ell k} r_j\right]_{,k}. \tag{45}$$

Integrating over the aggregate volume Ω^k and applying the divergence theorem yields

$$\int_{\Omega^k} \boldsymbol{P}^{m^k} \, \mathrm{d}V = \int_{\partial\Omega^k} \left(\boldsymbol{P}^{m^k} \boldsymbol{n}_k\right) \otimes \left(\boldsymbol{x}^m - \boldsymbol{X}_0^m\right) \mathrm{d}A, \tag{46}$$

where $\boldsymbol{n}_k$ is the outward unit normal on the aggregate surface. Since the aggregate surface coincides with the interfaces to the thin layers, tractions are continuous across these interfaces

$$\boldsymbol{P}^{m^k} \boldsymbol{n}_k = \boldsymbol{P}^{m^i} \boldsymbol{N}^i, \tag{47}$$

where $\boldsymbol{N}^i$ denotes the outward normal of layer Ω^i. Thus, the integral over the aggregate can be rewritten in terms of the layer tractions

$$\int_{\Omega^k} \boldsymbol{P}^{m^k} \, \mathrm{d}V = \sum_{i=1}^{m_{ml}} \int_{\partial\Omega^i} \left(\boldsymbol{P}^{m^i} \boldsymbol{N}^i\right) \otimes \left(\boldsymbol{x}^{m^i} - \boldsymbol{X}_0^m\right) \mathrm{d}A. \tag{48}$$

Substituting (48) into (42) gives

$$\boldsymbol{P}^{\mathcal{M}} = \frac{1}{V} \left[\sum_{i=1}^{m_{ml}} \int_{\Omega^i} \boldsymbol{P}^{m^i} \, \mathrm{d}V + \sum_{i=1}^{m_{ml}} \int_{\partial\Omega^i} \left(\boldsymbol{P}^{m^i} \boldsymbol{N}^i\right) \otimes \left(\boldsymbol{x}^{m^i} - \boldsymbol{X}_0^m\right) \mathrm{d}A \right]. \tag{49}$$

Based on the assumption of linear displacements and prismatic layers, leading to $V^i = A^i \cdot h^i$, $\boldsymbol{P}^{\mathcal{M}}$ can be represented as a linear mapping of $\boldsymbol{P}^i$

$$\boldsymbol{P}^{\mathcal{M}} = \sum_{i=1}^{m_{ml}} \frac{V^i}{V} \left[\mathbb{I} + \frac{1}{h^i} \mathbb{S}(\boldsymbol{x}^{m^i} - \boldsymbol{X}_0^m) \otimes \boldsymbol{N}^i \right] \boldsymbol{P}^{m^i} = \sum_{i=1}^{m_{ml}} \mathbb{K}^{m^i} : \boldsymbol{P}^{m^i}. \tag{50}$$

Here, $\mathbb{I}$ denotes the fourth-order identity tensor and $\mathbb{S}$ the fourth-order symmetrization tensor acting on second-order tensors, i.e., $(\mathbb{S} : \boldsymbol{A}) = \frac{1}{2}\left(\boldsymbol{A} + \boldsymbol{A}^{\mathsf{T}}\right)$. The macroscopic tangent $\mathbb{C}^{\mathcal{M}^P}$, fourth-rank tensor, is obtained by differentiating the constitutive equation as specified in (Equation (7))

$$\mathbb{C}^{\mathcal{M}^P} = \sum_{i=1}^{m_{ml}} \mathbb{K}^{m^i} : \frac{d\boldsymbol{P}^{m^i}}{d\boldsymbol{F}^{m^i}} : \frac{\partial \boldsymbol{H}^{m^i}}{\partial \boldsymbol{F}^{\mathcal{M}}} = \sum_{i=1}^{m_{ml}} \mathbb{K}^{m^i} : \mathbb{C}^{m^{i^P}} : \mathbb{A}^{m^i}, \tag{51}$$

with

$$\mathbb{A}^{m^i} = \frac{\partial \boldsymbol{H}^{m^i}}{\partial \boldsymbol{n}^i} \frac{\partial \boldsymbol{n}^i}{\partial \boldsymbol{F}^{\mathcal{M}}}. \tag{52}$$

It can be seen that the scale transition from the micro- to the macroscale proceeds via the composition of linear operators ($\mathbb{K}^{m^i}, \mathbb{C}^{m^{i^P}}, \mathbb{A}^{m^i}$, fourth-order tensors) acting on second-order fields. This enables the linearization required to solve the global system of equations.

3 | CONSTITUTIVE EQUATIONS ON THE MICROSCALE

3.1 | Intermediate configuration

Asphalt requires material models that include elastic and inelastic phenomena such as plasticity and viscosity. For such models, it is useful to split the deformation gradient multiplicatively by[4,20]

$$\boldsymbol{F} = \boldsymbol{F}^A \boldsymbol{F}^B. \tag{53}$$

The transformation properties are then carried over to the individual parts. This approach, rooted in the foundational contributions of Simo and Miehe[21,22,23], guarantees objectivity, thermodynamic consistency, and weak invariance under isochoric changes of the reference configuration. In the intermediate configuration, only the deformations caused by $\boldsymbol{F}^B$ are present[1]. In general, $\boldsymbol{F}$ is not a suitable deformation measure, as it also contains rigid body motions. Nevertheless, a major advantage of such a multiplicative decomposition is that it is accompanied by an additive decomposition of the Green-Lagrange deformation tensor $\boldsymbol{E}$[21]

$$\boldsymbol{E} = \boldsymbol{E}^A + \boldsymbol{E}^B = \frac{1}{2}(\boldsymbol{C}^A - \boldsymbol{I}) + \frac{1}{2}(\boldsymbol{C} - \boldsymbol{C}^A), \tag{54}$$

[1] All physical quantities used in Section 3 are defined on the microscale. For better readability, however, the index $\square^m$ has been omitted.

with

$$\boldsymbol{C}^A = \boldsymbol{F}^{\boldsymbol{A}^T}\boldsymbol{F}^{\boldsymbol{A}} = \boldsymbol{F}^{\boldsymbol{B}^{-T}}\boldsymbol{C}\boldsymbol{F}^{\boldsymbol{B}^{-1}}. \tag{55}$$

The right Cauchy-Green tensor $\boldsymbol{C} = \boldsymbol{F}^{\boldsymbol{T}}\boldsymbol{F}$ captures the quadratic deviation of line elements between the reference and the current configurations. It is therefore invariant under rigid body motions and serves as an important measure of deformation (objectivity). The spatial velocity gradient in the current configuration is defined as

$$\boldsymbol{l} = \operatorname{grad}(\dot{\boldsymbol{u}}) = \dot{\boldsymbol{F}}\,\boldsymbol{F}^{-1}. \tag{56}$$

l describes the local rate of change of the velocity field. Using Equation (53), time differentiation and the product rule give

$$\dot{\boldsymbol{F}} = \dot{\boldsymbol{F}}^A\,\boldsymbol{F}^B + \boldsymbol{F}^A\,\dot{\boldsymbol{F}}^B, \tag{57}$$

$$\boldsymbol{F}^{-1} = \left(\boldsymbol{F}^B\right)^{-1}\left(\boldsymbol{F}^A\right)^{-1}. \tag{58}$$

Hence,

$$\boldsymbol{l} = \dot{\boldsymbol{F}}^A\left(\boldsymbol{F}^A\right)^{-1} + \boldsymbol{F}^A\left(\dot{\boldsymbol{F}}^B\left(\boldsymbol{F}^B\right)^{-1}\right)\left(\boldsymbol{F}^A\right)^{-1}. \tag{59}$$

Pulling this quantity back to the intermediate configuration via $\boldsymbol{F}^A$ defines

$$\boldsymbol{L}^I := \left(\boldsymbol{F}^A\right)^{-1}\,\boldsymbol{l}\,\boldsymbol{F}^A, \tag{60}$$

and the corresponding intermediate-configuration contributions

$$\boldsymbol{L}^A := \left(\boldsymbol{F}^A\right)^{-1}\dot{\boldsymbol{F}}^A, \qquad \boldsymbol{L}^B := \dot{\boldsymbol{F}}^B\left(\boldsymbol{F}^B\right)^{-1}. \tag{61}$$

A direct substitution yields the additive decomposition in the intermediate configuration

$$\boldsymbol{L}^I = \boldsymbol{L}^A + \boldsymbol{L}^B. \tag{62}$$

Finally, the inelastic mapping evolves according to

$$\dot{\boldsymbol{F}}^B = \boldsymbol{L}^B\,\boldsymbol{F}^B, \tag{63}$$

which shows that the temporal evolution of inelastic phenomena (such as plasticity and viscosity) is governed entirely by $\boldsymbol{L}^B$ in the intermediate configuration and is independent of the elastic mapping $\boldsymbol{F}^A$ [20,21,23], and simplifies the identification and interpretation of material parameters using experimental data. Therefore, the dissipation inequality as the fundamental restriction in thermodynamics can be formulated relative to the intermediate configuration. The local dissipation

$$\mathcal{D}^{loc} = \mathcal{P}^I - \dot{\psi} \geq 0 \tag{64}$$

is expressed as a function of internal power density (stress power) $\mathcal{P}^I$ and the time derivative of the strain energy function ψ. The internal power in the intermediate configuration reads [22]

$$\mathcal{P}^I = \boldsymbol{\Sigma}^I : \boldsymbol{L}^I. \tag{65}$$

Using Equation (62), it follows

$$\mathcal{P}^I = \boldsymbol{\Sigma}^I : \boldsymbol{L}^A + \boldsymbol{\Sigma}^I : \boldsymbol{L}^B. \tag{66}$$

Following [23], it is assumed, that the free energy depends only on the elastic right Cauchy–Green tensor $\boldsymbol{C}^A$

$$\psi = \psi(\boldsymbol{C}^A). \tag{67}$$

The time derivative of the strain energy function is then expressed as

$$\dot{\psi} = \left[2\boldsymbol{C}^A\frac{\partial\psi}{\partial\boldsymbol{C}^A}\right] : \boldsymbol{L}^A = \frac{\partial\psi}{\partial\boldsymbol{C}^A} : \dot{\boldsymbol{C}}^A. \tag{68}$$

By rearranging Equation (64), this results in

$$\mathcal{D}^{\text{loc}} = \left[\boldsymbol{\Sigma}^I - 2\boldsymbol{C}^A\frac{\partial\psi}{\partial\boldsymbol{C}^A}\right] : \boldsymbol{L}^I + \left[2\boldsymbol{C}^A\frac{\partial\psi}{\partial\boldsymbol{C}^A}\right] : \boldsymbol{L}^B. \tag{69}$$

Equation (69) directly yields a computation rule for the Mandel stress tensor $\boldsymbol{\Sigma}^I$ in the intermediate configuration, but only if the assumption is made that purely $\boldsymbol{L}^B$ should cause dissipation

$$\boldsymbol{\Sigma}^I = 2\boldsymbol{C}^A\frac{\partial\psi}{\partial\boldsymbol{C}^A}. \tag{70}$$

$\boldsymbol{\Sigma}^I$ is defined as the work-conjugate quantity to the material evolution operator $\boldsymbol{L}^{\boldsymbol{B}}$, while itself depending only on non-dissipative quantities, making it fundamental for the modeling and computation of inelastic phenomena. The second Piola–Kirchhoff stress $\boldsymbol{S}$ as the stress measure conjugated to $\boldsymbol{E}$ and $\boldsymbol{C}$, defined by $\boldsymbol{S} = \dfrac{\partial \Psi}{\partial \boldsymbol{E}} = 2\,\dfrac{\partial \Psi}{\partial \boldsymbol{C}}$, is connected to the Mandel stress in the intermediate configuration via

$$\boldsymbol{\Sigma}^I = \boldsymbol{C}^A\,\boldsymbol{S}^I, \qquad \boldsymbol{S}^I = \boldsymbol{F}^B\,\boldsymbol{S}\,(\boldsymbol{F}^B)^{\mathsf{T}} = 2\,\frac{\partial \psi}{\partial \boldsymbol{C}^e}. \tag{71}$$

3.2 | Viscoelasticity

As shown in, the viscous deformations evolve relative to the intermediate configuration. Owing to the presence of stiffening aggregates in asphalt A portion of the compressive stresses remains unaffected by time. In order to take into account only the time-dependent part of the energy contribution due to viscous deformations ψ^v, only the part of the right Cauchy Green tensor where the elastic deformations have already occurred is used for their evolution $\boldsymbol{C}^e$ Based on the split introduced in Section 3.1 (Equation (53)), the evolution of viscous deformations is described in the intermediate configuration with $\boldsymbol{C}^e$ as the metric[21]. The underlying rheological model is a Maxwell element consisting of a viscous dashpot and an elastic spring. In parallel with an elastic branch, this yields a Zener model as proposed by Simo and Miehe[23]. The formulation is extended by[24] with an efficient time-stepping procedure. If k viscoelastic branches are included to capture multiple time scales, one obtains the generalized Maxwell model. Thus, in analogy to Equation (62), the free Helmholtz energy can be additively decomposed into its components

$$\psi = \psi^e(\boldsymbol{C}) + \sum_{w=1}^{k} \psi^{v,w}(\boldsymbol{C}^e). \tag{72}$$

Assume that the elastic material response is characterized by different behavior for purely volumetric and purely viscous deformations, the deformation gradient is multiplicatively split and, thus, the free Helmholtz energy is again additively decomposed into a volumetric and an isochoric part[20]

$$\psi = \psi^e_{iso}(\boldsymbol{C}_{\boldsymbol{iso}}) + \psi^e_{vol}(\det \boldsymbol{F}) + \sum_{w=1}^{k} \psi^{v,w}_{iso}(\boldsymbol{C}^e_{iso}), \tag{73}$$

with

$$\boldsymbol{C}_{\mathrm{iso}} = (\det \boldsymbol{F})^{-2/3}\boldsymbol{C}, \quad \boldsymbol{C}^e_{\mathrm{iso}} = (\det \boldsymbol{F}^e)^{-2/3}\boldsymbol{C}^e. \tag{74}$$

The viscous part is assumed to have no volumetric components[25,26,27,28]. For the subordinate volumetric part, the classic constitutive relationship

$$\psi^e_{vol} = \frac{\varkappa}{2}(\ln(\det(\boldsymbol{F})))^2 \tag{75}$$

is chosen. Due to the small number of material parameters to be determined and their suitability for finite strains, in this contribution, the Yeoh material model is used to describe the elastic isochoric part given by

$$\psi^e_{iso} = \sum_{i=1}^{3} c_i \left(\mathrm{tr}(\boldsymbol{C}_{iso}) - 3\right)^i. \tag{76}$$

The computation of the non-equilibrium energy $\psi^v_{iso}(\boldsymbol{C}^e_{iso})$ for the k viscoelastic chains also starts from the model given in Equation (76). The set of equivalent shear moduli $\tilde{c}_{i,w}$ for each chain w is scaled by

$$\tilde{c}_{i,w} = \alpha_w c_i. \tag{77}$$

With this, all contributions to the free Helmholtz energy are specified. The individual contributions to the viscoelastic part of the First Piola–Kirchhoff stress, ${}^{\mathrm{ve}}\boldsymbol{P}$, follow from Equation (6) as

$$\boldsymbol{P}^e_{\mathrm{vol}} = \frac{\partial \psi^e_{\mathrm{vol}}}{\partial \boldsymbol{F}} = \varkappa\,\ln\!\left(\det \boldsymbol{F}\right)\boldsymbol{F}^{-T}, \tag{78}$$

$$\boldsymbol{P}^e_{\mathrm{iso}} = 2\,\boldsymbol{F}\cdot\left(\frac{\partial \psi^e_{\mathrm{iso}}}{\partial \boldsymbol{C}_{\mathrm{iso}}} : \frac{\partial \boldsymbol{C}_{\mathrm{iso}}}{\partial \boldsymbol{C}}\right), \tag{79}$$

$$\boldsymbol{P}^{v,w}_{\mathrm{iso}} = \frac{\partial \psi^{v,w}_{\mathrm{iso}}}{\partial \boldsymbol{C}^{e,w}_{\mathrm{iso}}} : \frac{\partial \boldsymbol{C}^{e,w}_{\mathrm{iso}}}{\partial \boldsymbol{C}^{e,w}} : \frac{\partial \boldsymbol{C}^{e,w}}{\partial \boldsymbol{F}^{e,w}} : \frac{\partial \boldsymbol{F}^{e,w}}{\partial \boldsymbol{F}}. \tag{80}$$

The required derivatives are collected in the Appendix. The total viscoelastic stress ${}^{\text{ve}}\boldsymbol{P}$ is obtained as the sum of the elastic terms and the contributions from all viscous branches $w = 1, \dots, k$

$$ {}^{\text{ve}}\boldsymbol{P} = \boldsymbol{P}^{e}_{\text{vol}} + \boldsymbol{P}^{e}_{\text{iso}} + \sum_{w=1}^{k} \boldsymbol{P}^{v,w}_{\text{iso}}. \tag{81} $$

Analogously, the material tangents (Equation (7)) associated with ${}^{\text{ve}}\boldsymbol{P}$ read

$$ \mathbb{C}^{e}_{\text{vol}} = \frac{\partial \boldsymbol{P}^{e}_{\text{vol}}}{\partial \boldsymbol{F}} = \varkappa \left[\boldsymbol{F}^{-T} \otimes \boldsymbol{F}^{-T} - \ln\big(\det \boldsymbol{F}\big)\, \boldsymbol{F}^{-T} \otimes \big(\boldsymbol{F}^{-1}\boldsymbol{F}^{-1}\big) \right], \tag{82} $$

$$ \mathbb{C}^{e}_{\text{iso}} = \frac{\partial \boldsymbol{P}^{e}_{\text{iso}}}{\partial \boldsymbol{F}} = 2 \left[\mathbb{I} \cdot \left(\frac{\partial \psi^{e}_{\text{iso}}}{\partial \boldsymbol{C}_{\text{iso}}} : \frac{\partial \boldsymbol{C}_{\text{iso}}}{\partial \boldsymbol{C}} \right) + \boldsymbol{F} \cdot \left(\frac{\partial}{\partial \boldsymbol{F}} \left(\frac{\partial \psi^{e}_{\text{iso}}}{\partial \boldsymbol{C}_{\text{iso}}} : \frac{\partial \boldsymbol{C}_{\text{iso}}}{\partial \boldsymbol{C}} \right) \right) \right], \tag{83} $$

$$ \mathbb{C}^{v,w}_{\text{iso}} = \frac{\partial \boldsymbol{P}^{v,w}_{\text{iso}}}{\partial \boldsymbol{F}} = \frac{\partial}{\partial \boldsymbol{F}} \left(\frac{\partial \psi^{v,w}_{\text{iso}}}{\partial \boldsymbol{C}^{e,w}_{\text{iso}}} : \frac{\partial \boldsymbol{C}^{e,w}_{\text{iso}}}{\partial \boldsymbol{C}^{e,w}} : \frac{\partial \boldsymbol{C}^{e,w}}{\partial \boldsymbol{F}^{e,w}} \right), \tag{84} $$

and the total viscoelastic material tangent is

$$ {}^{\text{ve}}\mathbb{C} = \mathbb{C}^{e}_{\text{vol}} + \mathbb{C}^{e}_{\text{iso}} + \sum_{w=1}^{k} \mathbb{C}^{v,w}_{\text{iso}}. \tag{85} $$

The transformation of the first Piola-Kirchhoff stress tensor into the Mandel stress tensor is carried out by

$$ {}^{\text{ve}}\boldsymbol{\Sigma}^{I} = \boldsymbol{F}^{e^T} ({}^{\text{ve}}\boldsymbol{P}) \boldsymbol{F}^{v^T}. \tag{86} $$

In the case of viscoelasticity, both the Mandel stress ${}^{\text{ve}}\boldsymbol{\Sigma}^{I}$ and the viscous rate $\boldsymbol{L}^{v}$ are defined in the intermediate configuration I (see Section 3.1). In analogy to the formulation of[23] and subsequent developments in finite viscoelasticity[29,30,31], a linear flow rule is postulated. It reads in the intermediate configuration I

$$ \boldsymbol{L}^{v} = \mathbb{M} : {}^{\text{ve}}\boldsymbol{\Sigma}^{I}, \tag{87} $$

where $\mathbb{M}$ denotes a fourth-order viscosity operator acting in I. In line with linear irreversible thermodynamics[32], the viscous rate (flux) $\boldsymbol{L}^{v}$ is taken to be linear in its thermodynamic force ${}^{\text{ve}}\boldsymbol{\Sigma}^{I}$, and Onsager reciprocity implies the major symmetry and non-negativity,

$$ \mathbb{M} = \mathbb{M}^{\mathsf{T}} > 0. \tag{88} $$

This structure is consistent with finite strain models formulated on the intermediate configuration, where linear flow rules proportional to the stress are standard; see[23,29,30,32]. This completes the set of state equations. The specific choice is given in Table 1.

3.3 | Elastoplasticity

The definition of the free Helmholtz energy for plastic deformations follows in an analogous manner the considerations of Sections 3.1 and 3.2. Based on the multiplicative split of the deformation gradient according to Equation (53), and under the assumption that only elastic deformations induce stress while not causing any dissipative phenomena, the free Helmholtz energy, considering linear strain hardening of the material, is given by

$$ \psi = \psi^{e}(\boldsymbol{F}^{e}) + \psi^{\alpha} = \psi^{e} + \frac{1}{2}\alpha^{H^2} H. \tag{89} $$

Analogous to the viscoelastic chain, and employing the volumetric-isochoric split, Equations (73) and (76), one obtains

$$ \psi = \psi^{e}_{vol}(\boldsymbol{F}^{e}) + \psi^{e}_{iso}(\boldsymbol{C}^{e}_{iso}) + \frac{1}{2}\alpha^{H^2} H. \tag{90} $$

The neo-Hooke model is selected for the elastic parts

$$ \psi^{e}_{vol}(\boldsymbol{F}^{e}) = \frac{E}{6(1-2\nu)} \left(\ln(\det \boldsymbol{F}^{e})\right)^2 \tag{91} $$

and

$$ \psi^{e}_{iso}(\boldsymbol{C}^{e}_{iso}) = \frac{E}{4(1+\nu)} \left(\operatorname{tr}(\boldsymbol{C}^{e}_{iso}) - 3\right), \tag{92} $$

E denotes the Young's modulus and ν the Poisson's ratio. According to Equation (6), the sum of all elastic contributions to the First Piola–Kirchhoff stress, ${}^{p}\boldsymbol{P}$, is given by

$$\boldsymbol{P}^{e}_{\text{vol}} = \frac{\partial \psi^{e}_{\text{vol}}}{\partial \boldsymbol{F}} = \frac{\partial \psi^{e}_{\text{vol}}}{\partial (\det \boldsymbol{F}^{e})} \cdot \frac{\partial (\det \boldsymbol{F}^{e})}{\partial \boldsymbol{F}^{e}} : \frac{\partial \boldsymbol{F}^{e}}{\partial \boldsymbol{F}}, \tag{93}$$

$$\boldsymbol{P}^{e}_{\text{iso}} = \frac{\partial \psi^{e}_{\text{iso}}}{\partial \boldsymbol{F}} = \frac{\partial \psi^{e}_{\text{iso}}}{\partial \boldsymbol{C}^{e}_{\text{iso}}} : \frac{\partial \boldsymbol{C}^{e}_{\text{iso}}}{\partial \boldsymbol{C}^{e}} : \frac{\partial \boldsymbol{C}^{e}}{\partial \boldsymbol{F}^{e}} : \frac{\partial \boldsymbol{F}^{e}}{\partial \boldsymbol{F}}, \tag{94}$$

and

$${}^{p}\boldsymbol{P} = \boldsymbol{P}^{e}_{\text{vol}} + \boldsymbol{P}^{e}_{\text{iso}}, \tag{95}$$

Analogously, the associated material tangent Equation (7) reads

$$\mathbb{C}^{e}_{\text{vol}} = \frac{\partial^2 \psi^{e}_{\text{vol}}}{\partial \boldsymbol{F}\, \partial \boldsymbol{F}} = \frac{\partial}{\partial \boldsymbol{F}} \left(\frac{\partial \psi^{e}_{\text{vol}}}{\partial J^{e}} \cdot \frac{\partial J^{e}}{\partial \boldsymbol{F}^{e}} : \frac{\partial \boldsymbol{F}^{e}}{\partial \boldsymbol{F}} \right), \tag{96}$$

$$\mathbb{C}^{e}_{\text{iso}} = \frac{\partial^2 \psi^{e}_{\text{iso}}}{\partial \boldsymbol{F}\, \partial \boldsymbol{F}} = \frac{\partial}{\partial \boldsymbol{F}} \left(\frac{\partial \psi^{e}_{\text{iso}}}{\partial \boldsymbol{C}^{e}_{\text{iso}}} : \frac{\partial \boldsymbol{C}^{e}_{\text{iso}}}{\partial \boldsymbol{C}^{e}} : \frac{\partial \boldsymbol{C}^{e}}{\partial \boldsymbol{F}^{e}} : \frac{\partial \boldsymbol{F}^{e}}{\partial \boldsymbol{F}} \right), \tag{97}$$

and

$${}^{p}\mathbb{C} = \mathbb{C}^{e}_{\text{vol}} + \mathbb{C}^{e}_{\text{iso}}. \tag{98}$$

The required derivatives are collected in the Appendix. The thermodynamic driving force associated with hardening is calculated as

$$\boldsymbol{K} = -\frac{\partial \psi}{\partial \alpha^{H}} = -H \alpha^{H}. \tag{99}$$

The transformation of the first Piola-Kirchhoff stress tensor into the Mandel stress tensor is carried out by

$${}^{\text{p}}\boldsymbol{\Sigma}^{I} = \boldsymbol{F}^{e^{T}} ({}^{\text{p}}\boldsymbol{P}) \boldsymbol{F}^{\boldsymbol{v}^{T}}. \tag{100}$$

The evolution of plasticity is specified by a yield function

$$f_y \left({}^{p}\boldsymbol{\Sigma}^{I},\, \alpha^{H} \right) \;\leq\; 0, \tag{101}$$

and an associated plastic velocity gradient (both posed in the intermediate configuration I)

$$\boldsymbol{L}^{p} = \dot{\gamma}\, \frac{\partial f_y}{\partial {}^{p}\boldsymbol{\Sigma}^{I}}, \qquad \dot{\alpha}^{H} = -\dot{\gamma} \frac{\partial f_y}{\partial K}, \tag{102}$$

together with the Kuhn–Tucker conditions

$$\dot{\gamma} \geq 0, \qquad f_y \left({}^{p}\boldsymbol{\Sigma}^{I}, \alpha^{H} \right) \leq 0, \qquad \dot{\gamma}\, f_y \left({}^{p}\boldsymbol{\Sigma}^{I}, \alpha^{H} \right) = 0. \tag{103}$$

The full set of state equations is thus established, with the particular forms summarized in Table 1.

3.4 | Specific state equations for inelastic evolution

In Table 1, the evolution equations for multiplicative elasto-plasticity with von Mises plasticity are summarized[21,22] and compared with those for viscoelasticity[20], both formulated in the intermediate configuration I. In line with[23], the intermediate configuration is assumed isochoric, i.e., $\det \boldsymbol{F}^{B} = 1$. Under this assumption, the formulation satisfies *weak invariance*[24,30] with respect to unimodular changes of the reference configuration, provided the internal variables are transformed consistently. The equations are solved at each time step q by a local Newton–Raphson procedure, following[33], see also[4,20,31].

4 | NUMERICAL EXAMPLES

Subsequently, numerical examples are presented to demonstrate the capabilities of the proposed formulations. Throughout the following sections, in both the text and the figures, the terms stress and strain are used for simplicity. It should be noted that they refer to the true stresses (Cauchy stress tensor) and the engineering strains, respectively.

Viscosity		Plasticity	
Quantity	**Calculation**	**Quantity**	**Calculation**
Inelastic velocity gradient	$\boldsymbol{L}^{\upsilon} = \dot{\gamma}^{\upsilon}\boldsymbol{N}^{\upsilon}$	Plastic velocity gradient	$\boldsymbol{L}^{p} = \dot{\gamma}^{p}\frac{\partial f_y}{\partial \Sigma^I} = \dot{\gamma}^{p}\boldsymbol{N}^{p}$
		Flow rule	$f_y = \|\mathrm{dev}({}^{p}\boldsymbol{\Sigma}^I)\| - \sqrt{\frac{2}{3}}(\Sigma_0 + H\alpha^H) = 0$
		Flow direction	$\frac{\partial f_y}{\partial {}^{p}\boldsymbol{\Sigma}^I} = \frac{\mathrm{dev}({}^{p}\boldsymbol{\Sigma}^I)}{\|\mathrm{dev}({}^{p}\boldsymbol{\Sigma}^I)\|}$
Direction vector	$\boldsymbol{N}^{\upsilon} = \frac{\mathrm{dev}({}^{\mathrm{ve}}\boldsymbol{\Sigma}^I)}{\|\mathrm{dev}({}^{\mathrm{ve}}\boldsymbol{\Sigma}^I)\|}$	Direction vector	$\boldsymbol{N}^{p} = \frac{\mathrm{dev}({}^{p}\boldsymbol{\Sigma}^I)}{\|\mathrm{dev}({}^{p}\boldsymbol{\Sigma}^I)\|}$
inelastic strain rate	$\dot{\gamma}^{\upsilon} = \frac{1}{t_r}\left[\frac{\|\mathrm{dev}({}^{\mathrm{ve}}\boldsymbol{\Sigma}^I)\|}{\hat{\Sigma}}\right]$	Consistency parameter	$\boldsymbol{N}^{p} : {}^{p}\dot{\boldsymbol{\Sigma}}^I = \sqrt{\frac{2}{3}}H\dot{\gamma}^{p}$
Evolution equation	$\dot{\boldsymbol{F}}^{\upsilon} = \dot{\gamma}^{\upsilon}\boldsymbol{N}^{\upsilon}\boldsymbol{F}^{\upsilon}$	Evolution equation	$\dot{\boldsymbol{F}}^{p} = \dot{\gamma}^{p}\boldsymbol{N}^{p}\boldsymbol{F}^{p}$
Discretized evolution	$\boldsymbol{F}^{\upsilon}_{q+1} = -\exp[\Delta t\dot{\gamma}^{\upsilon}\boldsymbol{N}^{\upsilon}]\cdot\boldsymbol{F}^{\upsilon}_{q}$	Discretized evolution	$\boldsymbol{F}^{p}_{q+1} = -\exp[\dot{\gamma}^{p}\boldsymbol{N}^{p}]\cdot\boldsymbol{F}^{p}_{q}$

Table 1 Set of state equations for evolution of inelastic deformations.

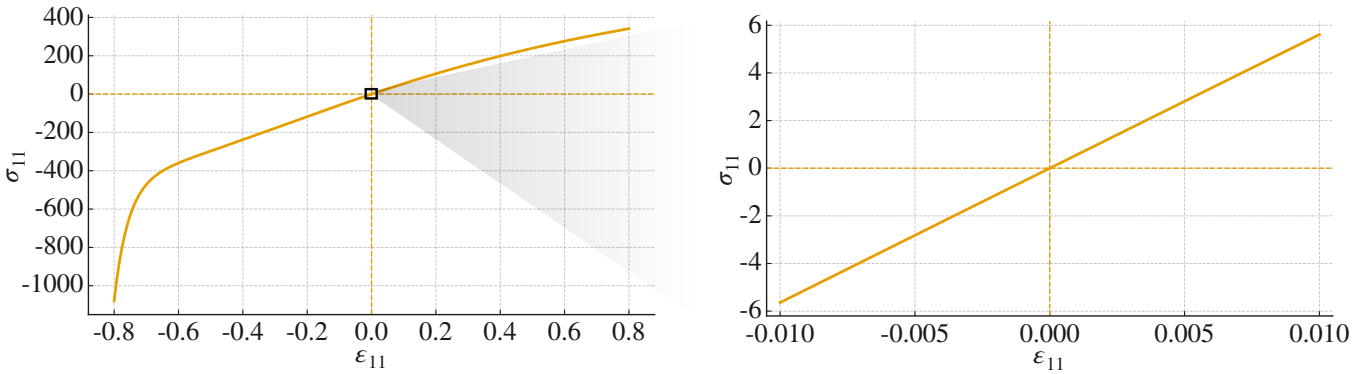

Figure 2 Schematic representation of the asymmetry between uniaxial tension and compression in the stress-strain behavior of a macroscopic Yeoh material model (Equations (75) and (76)) in case of finite strains ($\varkappa = 1000$ MPa, $c_1 = 100$ MPa, $c_2 = -10$ MPa, $c_3 = 1$ MPa).

4.1 | Tension-Compression Asymmetry

The tension and compression range of the stress-strain behavior of classical constitutive models at large elastic strains, such as the neo-Hooke or Yeoh material model, becomes increasingly asymmetrical with increasing load. Due to the small number of parameters, the validation of such models can be carried out directly by experiments. However, the asphalt material is subjected to strain levels that lie in the approximately symmetrical range of the stress-strain diagram, see Figure 2. A purely macroscopic use of the material models for the elastic components to map the tension-compression asymmetry of asphalt is, therefore, not feasible. This section will investigate whether this asymmetry can also be modeled for smaller strains with a suitable choice of the h^i/r^k ratio within the microlayer framework. For this purpose, simulations are carried out on cubes with an edge length of 150 mm

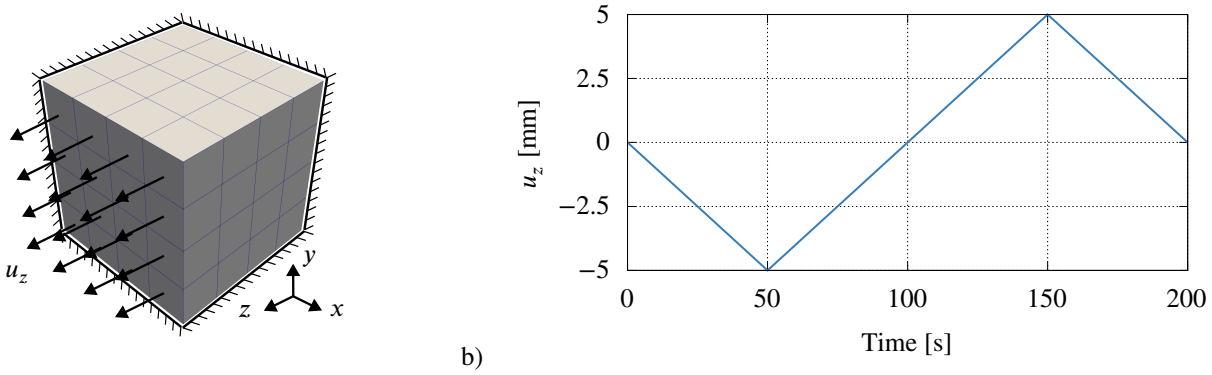

a) b)

Figure 3 a) Visualization of the boundary conditions and b) change in the Dirichlet boundary condition u_z over time.

Material parameter	**Value**	**Unit**
$\varkappa$	1000	MPa
c_1	100	MPa
c_2	−10	MPa
c_3	1	MPa
r^k	1	mm
m_{ml}	42	[-]
h^i	0.07 - 1	mm
Simulation parameter	**Value**	**Unit**
t_{tot}	200	s
$\lvert u_{z,max} \rvert$	5	mm

Table 2 Material and simulation parameters for the elastic Yeoh material model for each microlayer.

and a discretization of four elements per direction utilizing the Yeoh material model. All edge nodes that intersect the coordinate axes in $x_i = 0$ are each held in the x_i-direction. A Dirichlet boundary condition is applied by prescribing displacements at the upper surface along x_3-direction, see Figure 3a. In the first 50 seconds, a compression state is generated by reducing the height l_3 of the cube linearly by 5 mm using displacement boundary conditions. The direction of the displacements is then changed and the l_3 height of the cube is increased by 10 mm within 100 seconds. In the last time interval of 50 seconds, the l_3 height of the cube is deformed back to the initial height, see Figure 3b. The simulation ends after $t_{tot} = 200$ seconds. The selected material parameters are shown in Table 2. For the geometry of the microscale, a geometric transformation of the icosahedron is used for the aggregate Ω^k. By flattening the 12 corner points and simultaneously extracting the 30 edge centers, a polyhedron composed of 12 regular pentagonal and 30 regular hexagonal faces is formed, resulting in the number of microlayer of $m_{ml} = 42$. This has the advantage that the corner points of the resulting body all lie on a spherical surface, i.e. the aggregates are represented approximately as spheres. Due to symmetry properties, there are only 21 different microlayers to be analyzed. Figure 4 illustrates the stress-strain curve of the center node of the loaded plane in x_3-direction. It can be seen that the convexity of the nonlinear stress-strain curve typical for Yeoh model is maintained. During the homogenization at the transition from micro to macroscale, the original characteristic of the material model is thus preserved. Using Figure 5, it can be demonstrated that, under the selected boundary conditions, the macroscopic behavior for large ratios of h^i/r^k converges towards the solution of a purely macroscopic material model. Consequently, the asymmetry is only very weakly visible. As the h^i/r^k ratio decreases, the asymmetry increases non-linearly. With the microlayer framework, it is therefore possible to model materials where the stiffness properties differ greatly between tension and compression. In analogy to the real conditions of aggregate-matrix composites, this property is not generated purely artificially by the choice of a material model, but on the basis of the geometry at the microstructural level. In optimization algorithms for the identification of material parameters, it must be ensured by introducing a lower bound for the h^i/r^k ratio that there are no solution instabilities. This is due to the fact that the relationship between macroscopic strain and

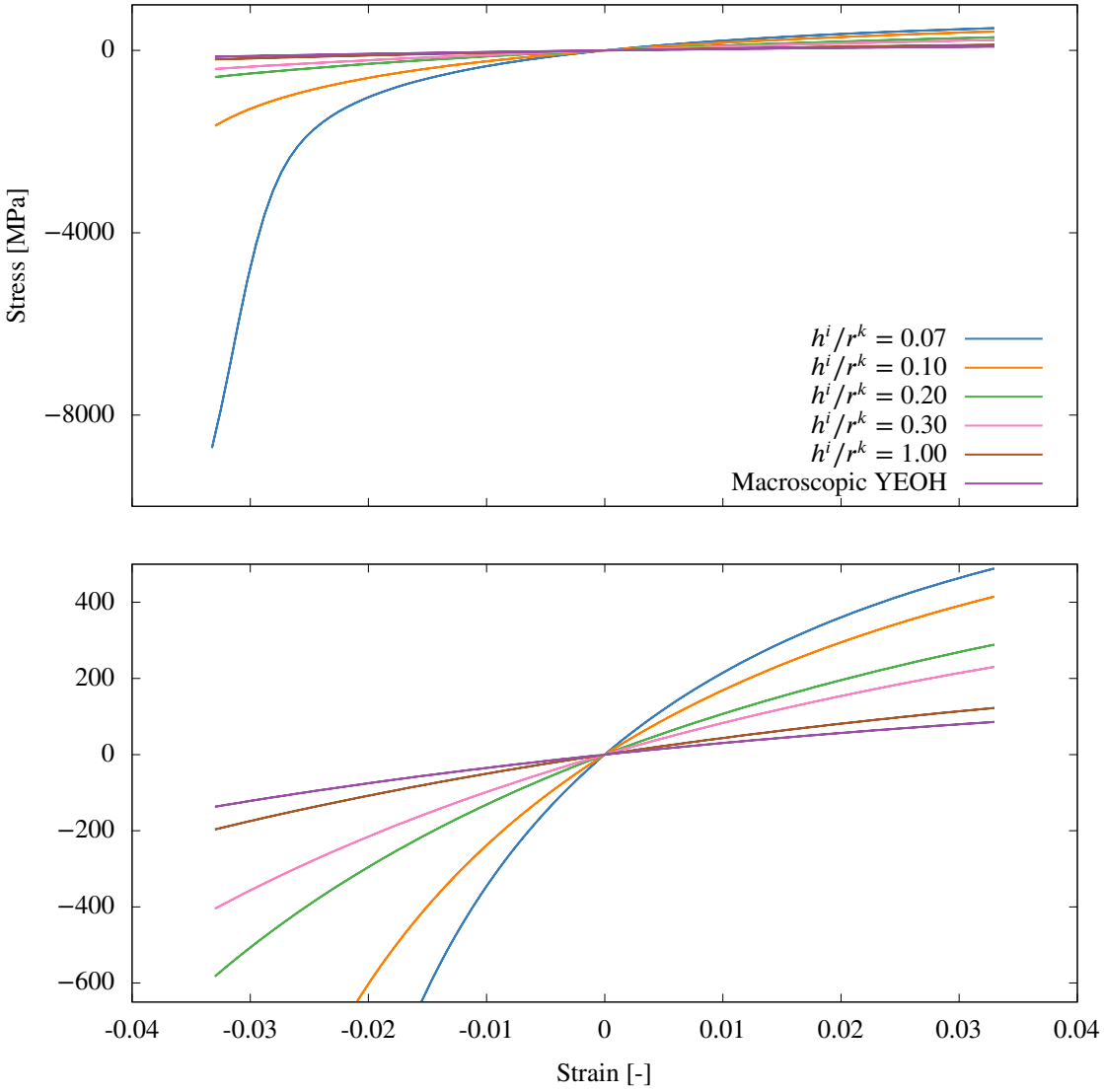

Figure 4 Influencing asymmetry between tension and compression area by adjusting layer height to aggregate radius rate h^i/r^k.

the resulting strain in a microlayer is inverse to each other. In the extreme case with $h^i/r^k \to 0$, there is then no volume left that can accommodate the macroscopic deformations.

4.2 | Viscoelasticity

With the specimen geometries and boundary conditions introduced in Section 4.1, simulations are carried out to characterize the viscous properties on a macroscopic level by adding two viscoelastic branches to the material model. On the one hand, it should be clarified whether physical properties are lost during the homogenization of the classical material models and whether additional effects can be meaningfully used for material modeling. The parameters of the purely elastic branch remain unchanged. The elastic part of the viscoelastic chain w is also implemented with the Yeoh material model, whereby the scalar α_w determines the ratio between the viscoelastic isochoric parameters $\tilde{c}_{p,w}$ and the isochoric elastic parameters c_p. To identify viscoelastic properties, α_1 and the duration t_{tot} of the compressive tensile load are varied for four different h^i/r^k ratio values. The total number of parameters used can be found in Table 3. The simulated stress-strain curves are shown in Figure 6. It can be seen that the distance between the loading and unloading path increases with decreasing retardation time. With slower load application ($t_{tot} = 600$ s), the separation between the loading and unloading paths is small for all investigated microlayer heights, showing only a minor

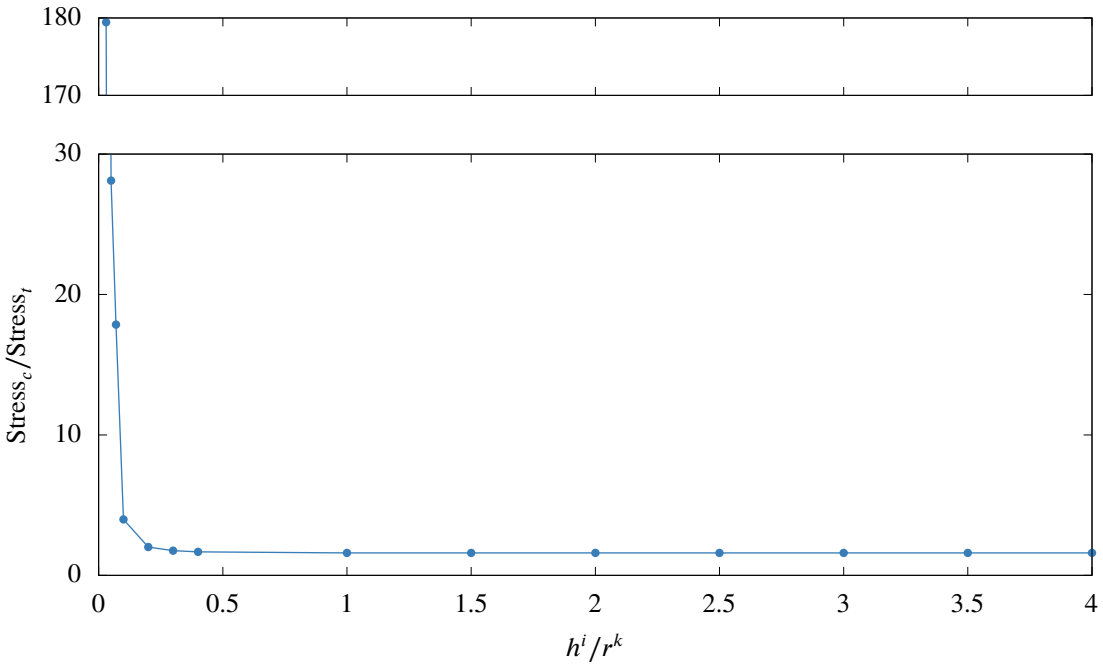

Figure 5 Evolution of the ratio of maximum compressive stress to maximum tensile stress with variation of the layer height to aggregate radius rate h^i/r^k.

Elastic material parameter	Value	Unit	Viscoelastic material parameter	Value	Unit
$\varkappa$	1000	MPa	α_1	8 - 32	[-]
c_1	100	MPa	α_2	2	[-]
c_2	-10	MPa	$t_{r,1}$	28556	s
c_3	1	MPa	$t_{r,2}$	24791	s
r^k	1	mm	$\hat{\Sigma}_1$	1	MPa
m_{ml}	42	[-]	$\hat{\Sigma}_2$	1	MPa
h^i	0.1 - 0.4	mm			
Simulation parameter					
t_{tot}	200 - 600	s			
$\lvert u_{z,max} \rvert$	5	mm			

Table 3 Material parameters for the mulitscale material model for viscoelasticity.

widening. The asymmetry of the stiffness properties for small h^i/r^k is retained. By increasing the isochoric elastic parameters in the first viscoelastic branch through an increase of the multiplier α_1, no significant changes are observed for the investigated microstructures, as the time-independent portion of the stress response remains large compared to the time-dependent portion. Reducing t_{tot} leads to a larger separation between the loading and unloading paths in the stress–strain behavior. Due to the shortened t_{tot}, the viscous chain cannot fully relax, leading to a behavior that is more strongly dominated by the viscous branch. The effect of the tension-compression asymmetry increases compared to the purely elastic model, as the delayed relaxation activates more asymmetric stiffness regions in the Yeoh model. If the stiffness in the viscous chain is also increased by increasing α_1, this effect is further intensified. This is evident from the fact that an abrupt unloading occurs even at small reverse strains. It can therefore be concluded that the essential physical properties of the Maxwell model are not lost during the scale transition to the macro level. In addition, the microlayer model offers the possibility of adjusting viscous properties not only by modifying

Elastic material parameter	Value	Unit	Viscoelastic material parameter	Value	Unit
$\varkappa$	1000	MPa	α_1	8 - 32	[-]
c_1	100	MPa	α_2	2	[-]
c_2	-10	MPa	$t_{r,1}$	0 - 26000	s
c_3	1	MPa	$t_{r,2}$	0 - 26000	s
r^k	1	mm	$\hat{\Sigma}_1$	1	MPa
m_{ml}	42	[-]	$\hat{\Sigma}_2$	1	MPa
h^i	0.05 - 0.5	mm	**Plastic material parameter**		
Simulation parameter			E	50000	MPa
t_{tot}	200	s	ν	0.2	[-]
$\lvert u_{z,max} \rvert$	2	mm	H	30	MPa
			Σ_0	500 - 10000	MPa

Table 4 Material parameters for the mulitscale material model for viscoelasticity with elastoplasticity

the material parameters, but also by tuning the ratio h^i/r^k. For an h^i/r^k ratio of 0.1, the path between the relief points loses C^1-continuity. However, these non-physical effects can be avoided by selecting a suitable lower limit for h^i/r^k.

4.3 | Plasticity and Viscoelasticity-Elastoplasticity

To investigate the plastic properties, the material model of the test specimen introduced in Sections 4.1 and 4.2 is extended by an elastoplastic branch. The effect of a neo-Hooke material model with von Mises plasticity and linear hardening on the macroscopic properties is first considered separately from the viscoelastic parts by numerically choosing zero retardation times $t_{r,i}$. The entirety of the material parameters can be taken from Table 4. Using Figure 7, it can be seen that with purely plastic simulations and low yield stress $\Sigma_0 = 500$ MPa, the typical approximately linear areas of elastic stiffness before and hardening after the yield point can be observed. However, the transition between the two areas is not sharp, but rather piecewise linear. At higher yield strengths Σ_0, the area of this transition zone widens. This is due to the fact that the yield point in the individual layers is reached with a load step shift, which is then macroscopically visible in an extended flow range. When the h^i/r^k ratio is reduced, high deformations are induced at the microscopic level, which result in the yield point being reached early in the heavily loaded microlayer after a few load steps. The loading and unloading paths are both non-linear and highly asymmetrical between the tensile and compressive areas. This indicates that not all microlayers are plasticized, because asymmetry and non-linearity are phenomena of the selected neo-Hooke model. By activating the viscoelastic branches, it can be seen for $h^i/r^k = 0.05$ that the yield point is reached later or not at all due to the time-delayed relaxation of these branches. The progress of the the stress-strain relation is determined by the plastic branch, therefore, no No noticeable difference between the loading and unloading branches can be observed for $\Sigma_0 = 10000$ MPa. If the h^i/r^k ratio is reduced with simultaneous activation of the viscoelastic branches, the already described effect of the asymmetry of the tensile-compression range and the strong non-linearity of the loading and unloading path occurs. However, the curves are stretched due to the time-delayed relaxation effect.

4.4 | Numerical simulation of a triaxial test for asphalt

In this Section, the microlayer framework will be examined with regard to its suitability as a material formulation for asphalt. In order to be able to simulate the vertical loads during a tire rollover and the associated horizontal confinement loads within the road in the laboratory, the triaxial test is used as a suitable laboratory experiment. For this purpose, a cylindrical sample is subjected to cyclic harmonic axial and radial stresses, see Figure 8.

4.4.1 | Experiment description

The triaxial testing apparatus at TU Dresden, which is shown in Figure 8b, enables the testing of cylindrical specimens with a diameter of 150 mm and a height of 300 mm under triaxial stress conditions. The cylindrical specimens are cored from plates previously compacted using a segmented rolling compactor and are subsequently ground to ensure parallel surfaces. To measure

node set or surface	fixed translation(s) u
border nodes in x-z plane	u_y
border nodes in y-z plane	u_x
top nodes	u_x, u_y
bottom nodes	u_z

Table 5 Boundary conditions for the finite element model of the triaxial test.

deformations, magnets are embedded into pre-drilled holes in the specimen using heated bitumen. The specimen is then mounted between a circular, rigid base plate and a circular, movable loading piston. To minimize friction between the specimen and both the base plate and the loading piston, a teflon sheet is inserted. A latex membrane is fitted around the specimen and coated with glycerol to reduce radial friction between the specimen and the pressure cell, and to protect the rubber membrane from premature damage. Following this, the base plate along with the specimen is lifted into the testing apparatus and secured to the frame. Vertical deformations are measured using a contactless magnetic measurement system. This system consists of three magnetic measuring stations, each containing two vertically aligned magnets. These stations are positioned at 120° intervals and located at heights of 75 mm and 225 mm above the base plate, respectively. The configuration is shown in Figure 9a. Vertical displacement of the magnetic field during specimen deformation is detected and converted into a measurement signal with a resolution of 0.001 mm. The advantage of this contactless method is that it enables direct measurement of axial deformation on the specimen itself, thereby eliminating the influence of vibrations from the testing setup or the measurement equipment. Radial deformations are recorded using a system consisting of nine inductive displacement transducers (Figure 9b). Three sensors are arranged at each of the three heights (75 mm, 150 mm, 225 mm) above the base plate. These sets of sensors are also spaced at 120° intervals. To avoid interference between the vertical and radial measurement systems, they are offset by 20° relative to each other. Prior to testing, the specimen is conditioned at the testing temperature of 25 °C for a minimum of six hours. Vertical loading is applied in the form of force-controlled, harmonic sinusoidal loading for a duration of 10 seconds, followed by a rest period of 60 seconds. A minimum stress of 0.075 MPa is applied to ensure the positioning of the specimen, while the maximum axial stress is set at 0.75 MPa. Radial loading is also applied in the form of force-controlled, harmonic sinusoidal loading followed by a rest period. The minimum radial stress, 0.075 MPa, ensures that the rubber membrane remains in contact with the specimen throughout the test, thus, maintaining radial confinement. The maximum radial stress is set at 0.5 MPa. The test frequency for both axial and radial loading is 10 Hz.

Due to machine-specific characteristics, there is a phase shift between the application of axial and radial maximum stresses. This shift is determined and compensated for in a preliminary test to ensure synchronized application of the peak axial and radial stresses. At a test duration of 10 seconds and a frequency of 10 Hz, a total of 100 loading cycles is applied vertically and radially at the beginning of the test. During the test, both axial and radial deformations are recorded. The applied vertical and radial stresses are shown in Figures 11 and 12 represents the post-loading residual stress necessary to ensure the sample's positional stability. Figures 13 and 14 present the resulting vertical strains. Radial strains could not be reliably evaluated due to interference in the measurement signal. As the radial deformation is measured through both the rubber and latex membranes, cyclic radial loading causes interaction between the membranes and the measurement system. This interaction becomes more pronounced with increasing confining pressure and significantly affects the accuracy of radial deformation measurements.

4.4.2 | Parameter identification

For parameter identification, the triaxial process described in Section 4.4.1 is numerically simulated multiple times as part of an evolution-based optimization process. The focus is on determining a deterministic solution. The inherent uncertainty in experiments with complex material composites should not and cannot be the subject of this contribution due to the limited number of measurement repetitions. The focus is also on the purely mechanical behavior at a constant temperature. Due to the symmetry properties of load in combination with the sample geometry, it is sufficient to simulate one eighth of the sample cylinder, see Figure 10. The selected boundary conditions correspond to those of the experiment and are shown Table 5. The axial strain is evaluated at the location of the transducer, see Figure 10. Based on preliminary tests on single-element samples in analogy to[2], essential ranges (Table 6) of the searched parameters are identified in order to enable optimization on the actual sample that is compatible with computing costs. Parameter identification is posed as a constrained least–squares problem. The

Elastic material param.	Value	Range	Unit	Viscoelastic material param.	Value	Range	Unit
$\varkappa$	24.3	1 - 1000	MPa	α_1	45.6	1 - 50	[-]
c_1	31.5	1 - 1000	MPa	α_2	5.1	1 - 10	[-]
c_2	−99.4	(−100) - (−0.1)	MPa	$t_{r,1}$	5114	1 - 50000	s
c_3	34.3	0.1 - 40	MPa	$t_{r,2}$	48012	1 - 50000	s
r^k	0.5	0.2 - 1.4	mm	$\hat{\Sigma}_1$	1	-	MPa
m_{ml}	42	-	[-]	$\hat{\Sigma}_2$	1	-	MPa
h^i	1	-	mm	**Plastic material param.**			
Simulation param.				E	25000	10000 - 40000	MPa
t_{tot}	70	-	s	ν	0.22	0.2 - 0.45	[-]
				H	5000	100 - 50000	MPa
				Σ_0	1.4	0.1 - 100	MPa

Table 6 Material parameters for the multiscale material model for viscoelasticity with elastoplasticity. For the parameters determined by optimization, the search space for the individual parameters determined in preliminary tests is also specified.

objective uses only the time–averaged mean–squared error (MSE) between simulated and experimental strain histories. The MSE quantifies the average squared deviation between the numerically computed and experimentally measured strains ε_{zz} over the total number N of experimental data points i

$$\mathrm{MSE} = \frac{1}{N}\sum_{i=1}^{N}\left(\varepsilon_{zz,i}^{\mathrm{num}} - \varepsilon_{zz,i}^{\mathrm{exp}}\right)^2. \tag{104}$$

A Poisson lower bound guarantees a physically admissible stress-strain behavior (no auxetic response). In the present setting, the volumetric contribution stems from the purely elastic branches (plastic equilibrium branch and an additional elastic parallel spring), so the initial effective bulk modulus reads

$$\varkappa_0 = \varkappa_{\mathrm{pl}} + \varkappa, \tag{105}$$

(Maxwell branches assumed isochoric). The instantaneous shear modulus collects all isochoric springs that carry stress at $t = 0$

$$\mu_0 \;=\; \mu_{\mathrm{pl}} + \mu_{\mathrm{el}} + \sum_{i=1}^{2}\mu_i. \tag{106}$$

It holds $\mu_{pl} = \frac{E}{2(1+\nu)}$, $\varkappa_{pl} = \frac{E}{3(1-2\nu)}$ and for the elastic spring $\mu_{el} = 2c_1$. For the other isochoric Yeoh springs, the instantaneous shear moduli are $\mu_i = 2\alpha_i c_1$. A Poisson lower bound is enforced

$$R_{\min} - \frac{K_0}{\mu_0} \;\le 0, \qquad R_{\min} \;=\; \frac{2(1+\nu_{\min})}{3(1-2\nu_{\min})}. \tag{107}$$

This guarantees $\nu_{\mathrm{eff}} \ge \nu_{\min}$ for the initial tangent and prevents auxetic behavior. The value $\nu_{\min} = 0.2$ is chosen following [34]. For the optimization procedure, the covariance matrix adaptation evolution strategy (CMA-ES) [35] is selected. CMA-ES is appropriate in this setting because it is derivative-free and due to the expected correlations, i.e., mutual influences between parameters of individual branches as it learns the covariance structure of the search distribution and effectively accounts for (and reduces the impact of) such correlations. The parameter identification of the $n = 13$ parameters (Table 6) was carried out using the `pymoo` [36] tool. The algorithm was initialized with an initial mean vector `x0` defined by the optimal parameter values obtained from the single-element test. It corresponds to the mean value within the parameter ranges specified in Table 6. An initial standard deviation of `sigma` $= 0.2$, and a population size of `pop_size` $= 4 + \lfloor 3\ln(n) \rfloor = 10$ is used. To enhance global exploration, `restarts` $= 3$ were employed. The parameters to be optimized are shown Table 6. The mean square error is $\mathrm{MSE} = 3.53 \cdot 10^{-10}$. The microlayer framework is capable of realistically mapping the complex multiaxial stress states under high-frequency tire loads. In the unloading regime, the simulated curve is not smooth and partially deviates from the experimental curve, because the simulation employs the exact load amplitudes recorded in the experiment. To ensure positional stability, a residual stress is always present even in the nominally load-free interval. This residual stress is machine-induced and therefore not constant; it fluctuates, culminating in a slightly unstable relaxation phase.

5 | CONCLUSION AND OUTLOOK

In the present contribution, it is demonstrated that the inherent asymmetry between the macroscopic compressive and tensile behavior in aggregate-matrix composites can be represented by choosing an RVE geometry that closely resembles the natural structure of an aggregate-matrix composite. The major advantage of this approach is the ability to use classical constitutive models developed for isotropic material behavior. Reflecting real-world conditions, the asymmetry as well as the anisotropy arise from the microstructural geometry, not from the materials themselves. Nevertheless, the characteristics of the employed Yeoh model are preserved during the scale transition.

The composition of the microstructure is based on simple geometric shapes, which means that the variational problem of the microstructure is directly available in analytical form. This makes the microlayer framework numerically more efficient than FE^2 approaches.

In this study, the behavior is investigated purely mechanically. Adding a coupled temperature degree of freedom is also easily possible on the microstructural level, since established thermomechanical approaches can be used and homogenization via the PMVP can be suitably developed. Particularly interesting is the addition of nonlocal damage formulations, as the presented framework allows for damage evolution to be induced separately for each microlayer. The result is an anisotropic damage evolution, as observed in asphalt due to unidirectional mechanical loading and strong temperature gradients along the depth direction.

During hot asphalt paving, a preferred orientation of the anisotropic aggregates can be observed. The aggregates, which often have a pronounced longitudinal shape, tend to settle horizontally within the road structure. By employing anisotropic aggregate structures, which can be realized within the microlayer framework, the impact of this phenomenon on macroscopic mechanical properties can be explored.

A significant disadvantage of the well-known microplane model is its incorrect stress-strain behavior outside the direction in which the parameters were identified, especially under multiaxial stress states. Since the microlayer model uses fully tensorial formulations for the material behavior, it is well-suited for validating asphalt under complex, multiphysical loading conditions.

So far, there is no true triaxial laboratory test available for asphalt where parameters for a material model can be identified in one direction and then validated in the others. The presented triaxial test is, due to the sample geometry and loading regime, only biaxial. Since strains in the radial direction cannot be determined with sufficient accuracy, a validation of the obtained parameters is not possible. A novel true triaxial test stand, which has not yet been documented in the literature, uses a cubic asphalt specimen and allows independent loading in all three spatial directions. Such a setup would be especially interesting. In contrast to the triaxial test, it would be possible to generate purely hydrostatic stress states and thereby directly determine the time-independent volumetric elastic parameters. This reduces the number of unknowns in the subsequent optimization for identifying the material parameters.

ACKNOWLEDGMENT

The present contribution has been developed under the research project No. 453596084 (SFB/TRR 339 Project A01, A06) and under project No. 414936990 (KA 1163/46-2), which has been granted by the German Research Foundation (Deutsche Forschungsgemeinschaft). The financial support of the German Research Foundation is gratefully acknowledged.

Competing interests

The authors declare that they have no known competing interests that could have appeared to influence the work reported in this paper.

Funding

This contribution is funded by the German Research Foundation (Deutsche Forschungsgemeinschaft) under the project No. 453596084 (SFB/TRR 339 Project A01, A06) and under project No. 414936990 (KA 1163/46-2).

Availability of data and materials

The data that support the findings of this study are available from the corresponding author upon reasonable request.

Authors contribution

Marcel May: Writing - Original draft, Visualization, Software, Methodology, Conceptualization.
Jakob Platen: Software, Writing - Review and Editing, Methodology. Ines Wollny: Conceptualization, Writing - Review and Editing, Project administration, Supervision. Erik Kamratowsky and Gustavo Canon Fella: Resources, Investigation, Writing - Original Draft. Alexander Zeißler and Michael Kaliske: Supervision, Project administration, Funding acquisition, Writing - Review and Editing.

How to cite this article: M. May, J. Platen, E. Kamratowsky, G. C. Falla, I. Wollny, A. Zeißler, M. Kaliske (20XX), Microlayer Model: A nonlinear finite strain viscoelastoplastic formulation for asphalt, *International Journal for Numerical Methods in Engineering*, *XXXX;XX:XX–XX*.

APPENDIX

Partial derivatives for the derivation of $^{\square}\boldsymbol{P}$ and $^{\square}\mathbb{C}$ at the microstructural level using the neo-Hookean material model for elastoplasticity $^{\mathrm{p}}\square$ and the Yeoh material model for viscoelasticity $^{\mathrm{ve}}\square$. $\mathbb{I}$ denotes the fourth-order identity tensor, $\mathbb{S}$ the fourth-order symmetrization tensor.

Viscoelasticity

$$\frac{\partial \psi^{e}_{iso}}{\partial \boldsymbol{C}_{iso}} = \sum_{i=1}^{3} i c_i \left(\mathrm{tr}(\boldsymbol{C}_{iso}) - 3\right)^{i-1} \boldsymbol{I} \tag{1}$$

$$\frac{\partial \boldsymbol{C}_{iso}}{\partial \boldsymbol{C}} = (\det \boldsymbol{F})^{-2/3} \left(\boldsymbol{I} - \frac{1}{3}\boldsymbol{C}^{-1} \otimes \boldsymbol{C}\right) \tag{2}$$

$$\frac{\partial \psi^{v}_{iso}}{\partial \boldsymbol{C}^{e}_{iso}} = \sum_{i=1}^{3} i \tilde{c}_i \left(\mathrm{tr}(\boldsymbol{C}^{e}_{iso}) - 3\right)^{i-1} \boldsymbol{I} \tag{3}$$

$$\frac{\partial \boldsymbol{C}^{e}_{iso}}{\partial \boldsymbol{C}^{e}} = (\det \boldsymbol{F}^{e})^{-2/3} \left(\boldsymbol{I} - \frac{1}{3}\boldsymbol{C}^{e} \otimes \boldsymbol{C}^{e^{-1}}\right) \tag{4}$$

$$\frac{d\boldsymbol{C}^{e}}{d\boldsymbol{F}} = \boldsymbol{F}^{v^{-T}} \cdot \boldsymbol{F}^{e} + (\boldsymbol{F}^{e})^{T} \cdot \boldsymbol{F}^{v^{-1}} \tag{5}$$

$$\frac{d}{d\boldsymbol{F}}\left(\frac{\partial \boldsymbol{C}_{iso}}{\partial \boldsymbol{C}}\right) = -\frac{2}{3}(\det \boldsymbol{F})^{-2/3} \cdot \boldsymbol{F}^{-T} \otimes \left(\boldsymbol{I} - \frac{1}{3}\boldsymbol{C}^{-1} \otimes \boldsymbol{C}\right) + (\det \boldsymbol{F})^{-2/3} \cdot \frac{d}{d\boldsymbol{F}}\left(-\frac{1}{3}\boldsymbol{C}^{-1} \otimes \boldsymbol{C}\right) \tag{6}$$

$$\frac{d}{d\boldsymbol{F}}\left(-\frac{1}{3}\boldsymbol{C}^{-1} \otimes \boldsymbol{C}\right) = \frac{2}{3}\left[\boldsymbol{C}^{-1} \cdot \boldsymbol{F} \cdot \boldsymbol{C}^{-1} \otimes \boldsymbol{C} - \boldsymbol{C}^{-1} \otimes \boldsymbol{F}\right] \tag{7}$$

$$\frac{d}{d\boldsymbol{F}}\left(\frac{\partial \psi^{e}_{iso}}{\partial \boldsymbol{C}_{iso}}\right) = \sum_{i=2}^{3} i(i-1) c_i \left(\mathrm{tr}(\boldsymbol{C}_{iso}) - 3\right)^{i-2} \cdot \left(\frac{d\,\mathrm{tr}(\boldsymbol{C}_{iso})}{d\boldsymbol{F}}\right) \otimes \boldsymbol{I} \tag{8}$$

$$\frac{d\,\mathrm{tr}(\boldsymbol{C}_{iso})}{d\boldsymbol{F}} = \frac{d(\det \boldsymbol{F})^{-2/3}}{d\boldsymbol{F}} : \boldsymbol{C} + (\det \boldsymbol{F})^{-2/3} \cdot \frac{d\boldsymbol{C}}{d\boldsymbol{F}} \tag{9}$$

$$\frac{d(\det \boldsymbol{F})^{-2/3}}{d\boldsymbol{F}} = -\frac{2}{3}(\det \boldsymbol{F})^{-2/3}\, \boldsymbol{F}^{-T} \tag{10}$$

$$\frac{d}{d\boldsymbol{F}}\left(\frac{\partial \psi^{v}_{iso}}{\partial \boldsymbol{C}^{e}_{iso}}\right) = \sum_{i=2}^{3} i(i-1) \tilde{c}_i \left(\mathrm{tr}(\boldsymbol{C}^{e}_{iso}) - 3\right)^{i-2} \cdot \left(\frac{d\,\mathrm{tr}(\boldsymbol{C}^{e}_{iso})}{d\boldsymbol{F}}\right) \otimes \boldsymbol{I} \tag{11}$$

$$\frac{d}{d\boldsymbol{F}}\left(\frac{\partial \boldsymbol{C}^{e}_{iso}}{\partial \boldsymbol{C}^{e}}\right) = \frac{d(\det \boldsymbol{F}^{e})^{-2/3}}{d\boldsymbol{F}} \otimes \left(\boldsymbol{I} - \frac{1}{3}\boldsymbol{C}^{e} \otimes (\boldsymbol{C}^{e})^{-1}\right) + (\det \boldsymbol{F}^{e})^{-2/3} \cdot \frac{d}{d\boldsymbol{F}}\left(-\frac{1}{3}\boldsymbol{C}^{e} \otimes (\boldsymbol{C}^{e})^{-1}\right) \tag{12}$$

$$\frac{d}{d\boldsymbol{F}}\left(-\frac{1}{3}\boldsymbol{C}^e \otimes (\boldsymbol{C}^e)^{-1}\right) = -\frac{1}{3}\left[\left(\frac{d\boldsymbol{C}^e}{d\boldsymbol{F}}\right) \otimes (\boldsymbol{C}^e)^{-1} - \boldsymbol{C}^e \otimes \left((\boldsymbol{C}^e)^{-1} \cdot \left(\frac{d\boldsymbol{C}^e}{d\boldsymbol{F}}\right) \cdot (\boldsymbol{C}^e)^{-1}\right)\right] \tag{13}$$

$$\frac{d^2\boldsymbol{C}^e}{d\boldsymbol{F}^2} = 2 \cdot (\boldsymbol{F}^{v^{-1}})^T \otimes \boldsymbol{F}^{v^{-1}} \tag{14}$$

Elastoplasticity

$$\frac{\partial \psi^e_{vol}}{\partial(\det \boldsymbol{F}^e)} = \frac{E}{3(1-2\nu)} \ln(\det \boldsymbol{F}^e) \tag{15}$$

$$\frac{\partial(\det \boldsymbol{F}^e)}{\partial \boldsymbol{F}^e} = (\det \boldsymbol{F}^e) \cdot (\boldsymbol{F}^e)^{-T} \tag{16}$$

$$\frac{\partial \boldsymbol{F}^e}{\partial \boldsymbol{F}} = \mathbb{I} \otimes \boldsymbol{F}^{p^{-1}} \tag{17}$$

$$\frac{\partial \psi^e_{iso}}{\partial \boldsymbol{C}^e_{iso}} = \frac{E}{4(1+\nu)}\boldsymbol{I} \tag{18}$$

$$\frac{\partial \boldsymbol{C}^e_{iso}}{\partial \boldsymbol{C}^e} = (\det \boldsymbol{F}^e)^{-2/3}\left(\mathbb{I} - \frac{1}{3}\boldsymbol{C}^e \otimes \boldsymbol{C}^{e^{-1}}\right) \tag{19}$$

$$\frac{\partial \boldsymbol{C}^e}{\partial \boldsymbol{F}^e} = 2\,\mathbb{S} \cdot \boldsymbol{F}^e \tag{20}$$

$$\frac{\partial^2 \psi^e_{vol}}{\partial(\det \boldsymbol{F}^e)\partial(\det \boldsymbol{F}^e)} = \frac{E}{3(1-2\nu)} \cdot \frac{1}{(\det \boldsymbol{F}^e)} \tag{21}$$

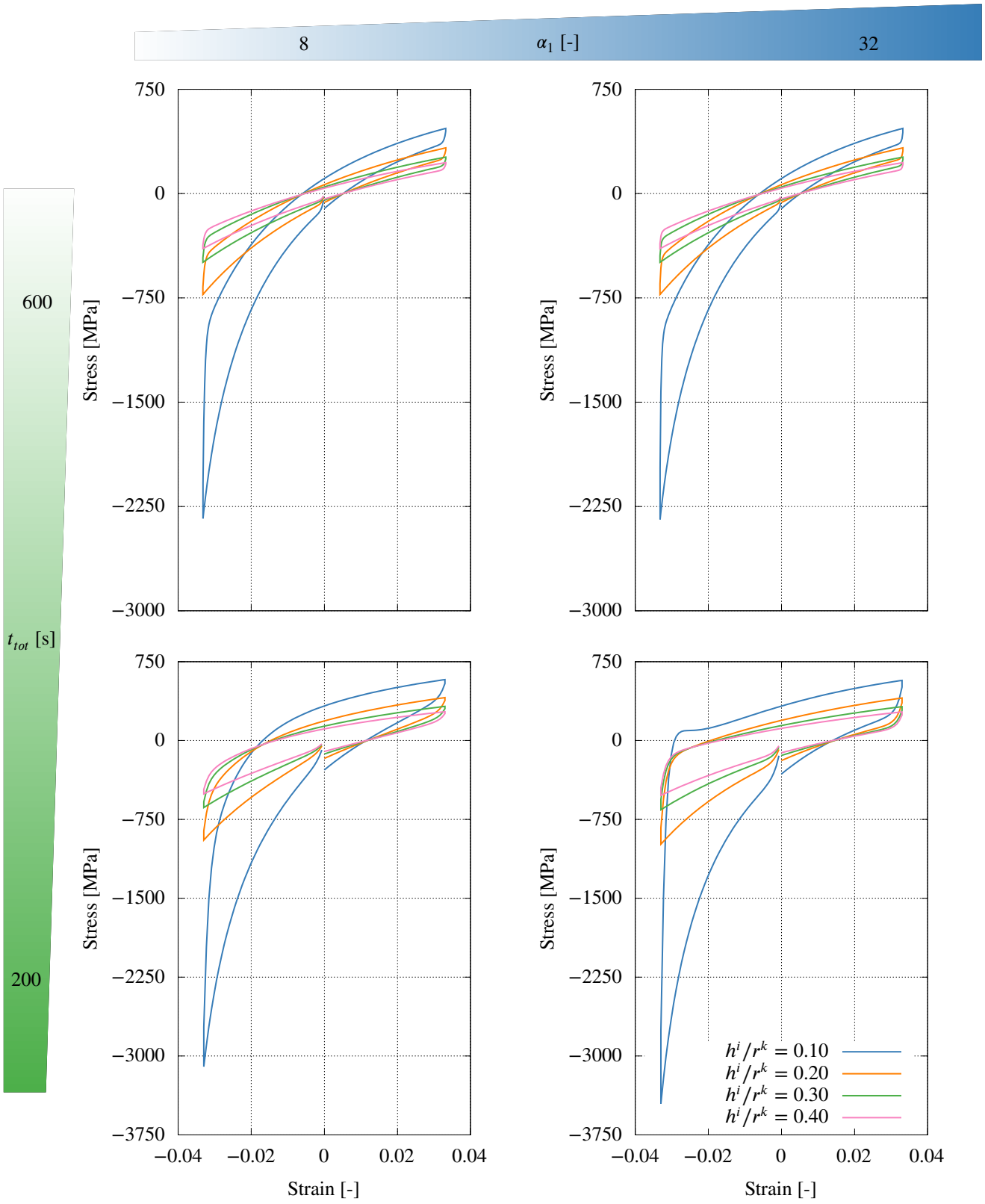

Figure 6 Influencing the viscoelastic stress-strain behavior by lowering the simulation time (from top to bottom) and increasing the ratio of the isochoric viscoelastic parameters to the pure elastic parameters (from left to right).

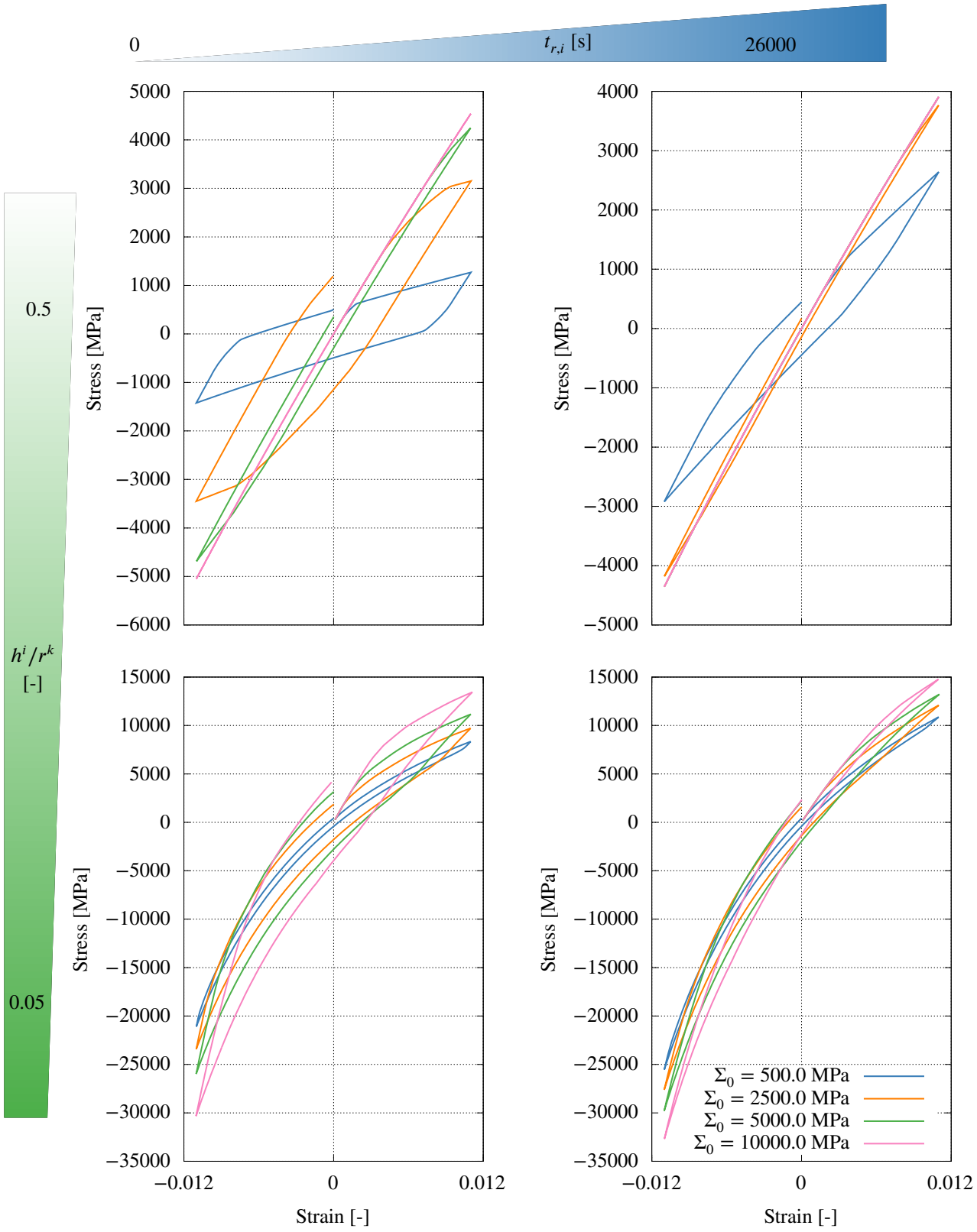

Figure 7 Influencing the plastic stress-strain behavior by reducing the ratio h^i/r^k (from top to bottom) and enabling viscoelastic-elastoplastic behavior by increasing the retardation times $t_{r,i}$ (from left to right).

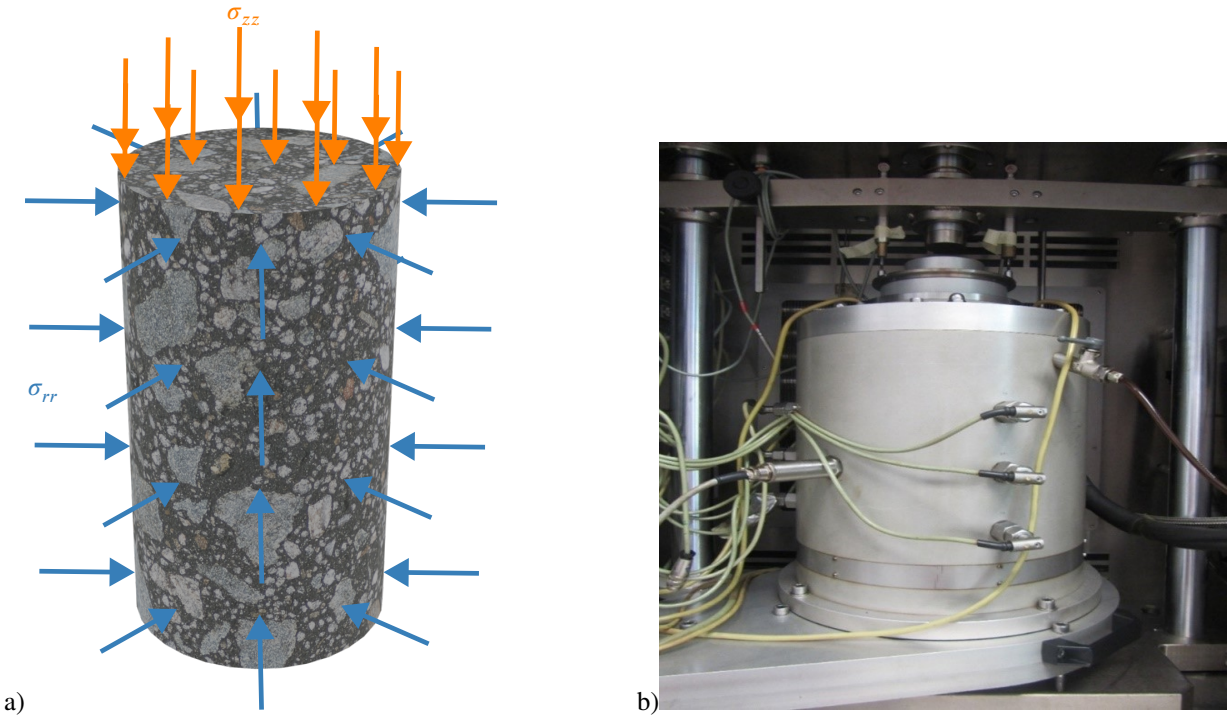

Figure 8 Illustration of a) the loaded triaxial specimen and b) the triaxial testing apparatus.

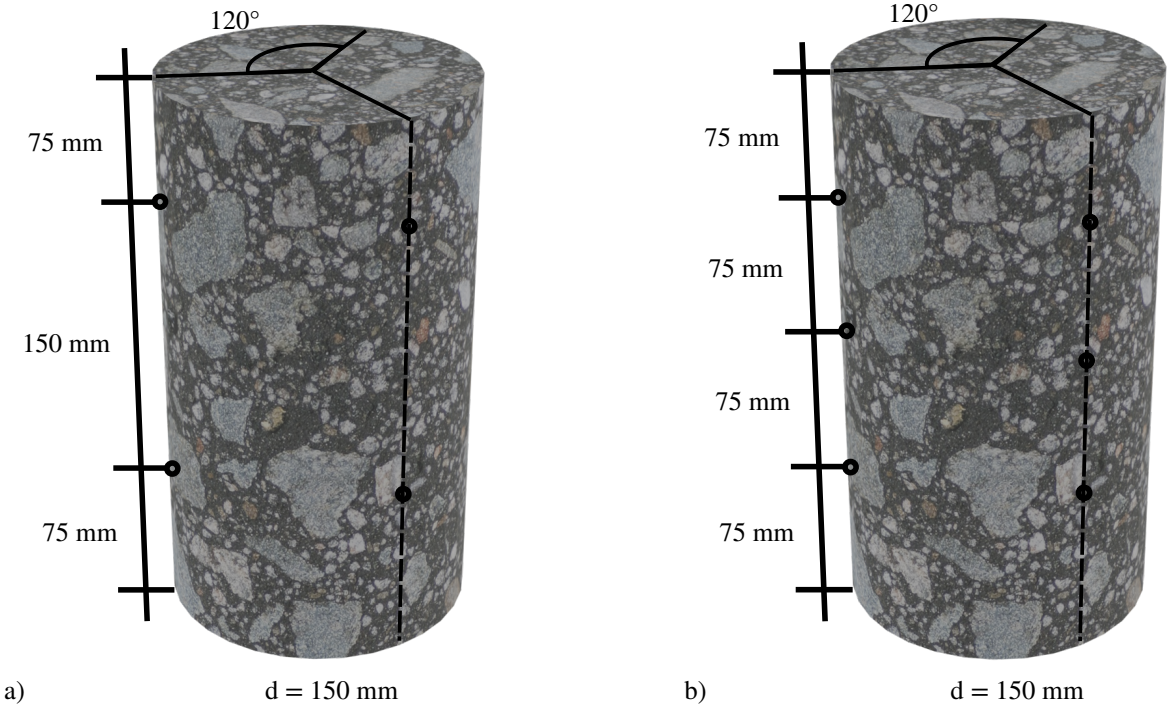

Figure 9 Positions of the a) axial and b) radial measurement sensors.

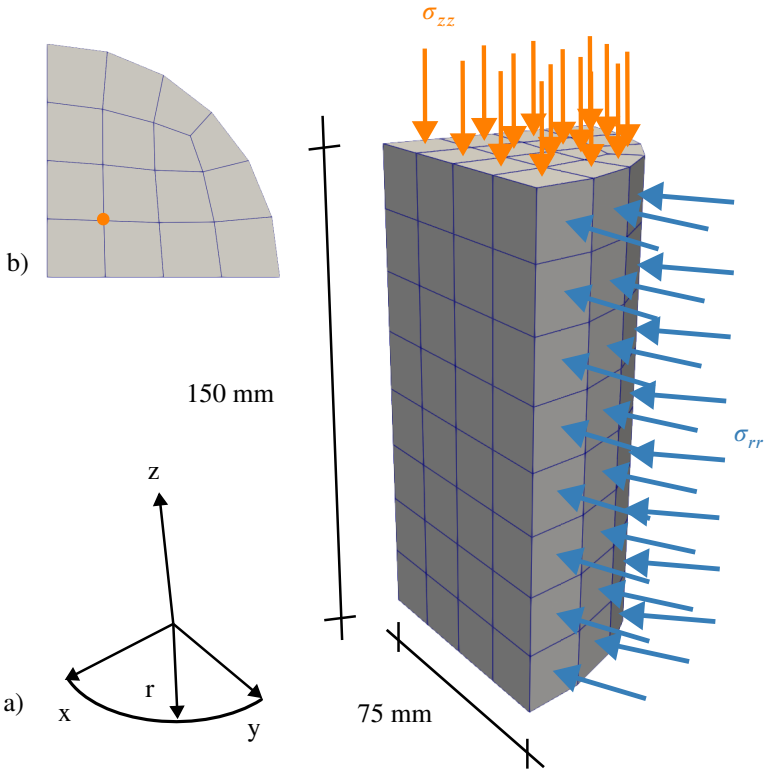

Figure 10 Illustration of a) discretization of the triaxial specimen with reduced volume for symmetry reasons and b) evaluated node on the specimen surface.

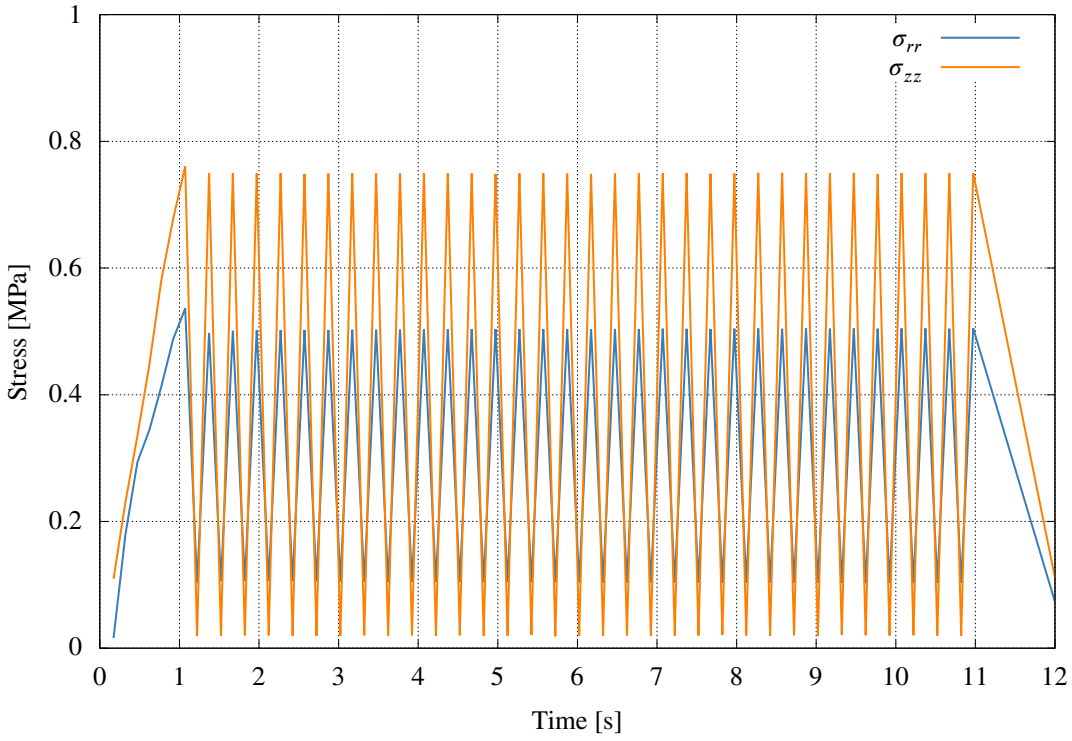

Figure 11 Temporal evolution of radial and axial loading of the specimen in simulation and experiment.

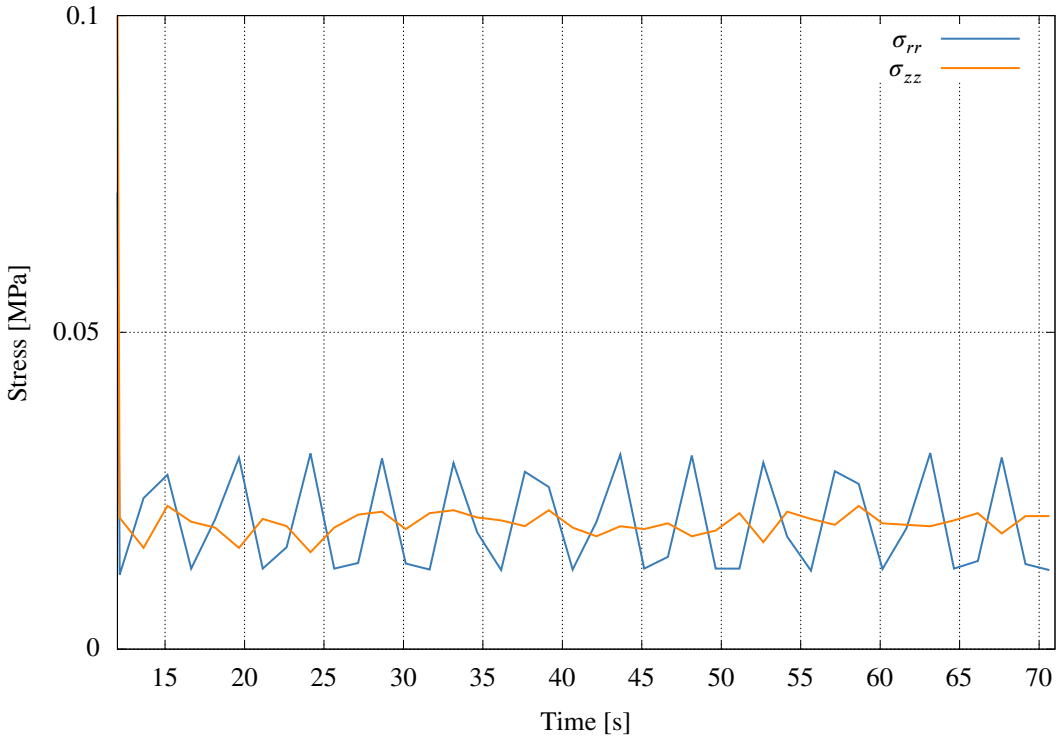

Figure 12 Post-loading residual stress necessary to ensure the sample's positional stability.

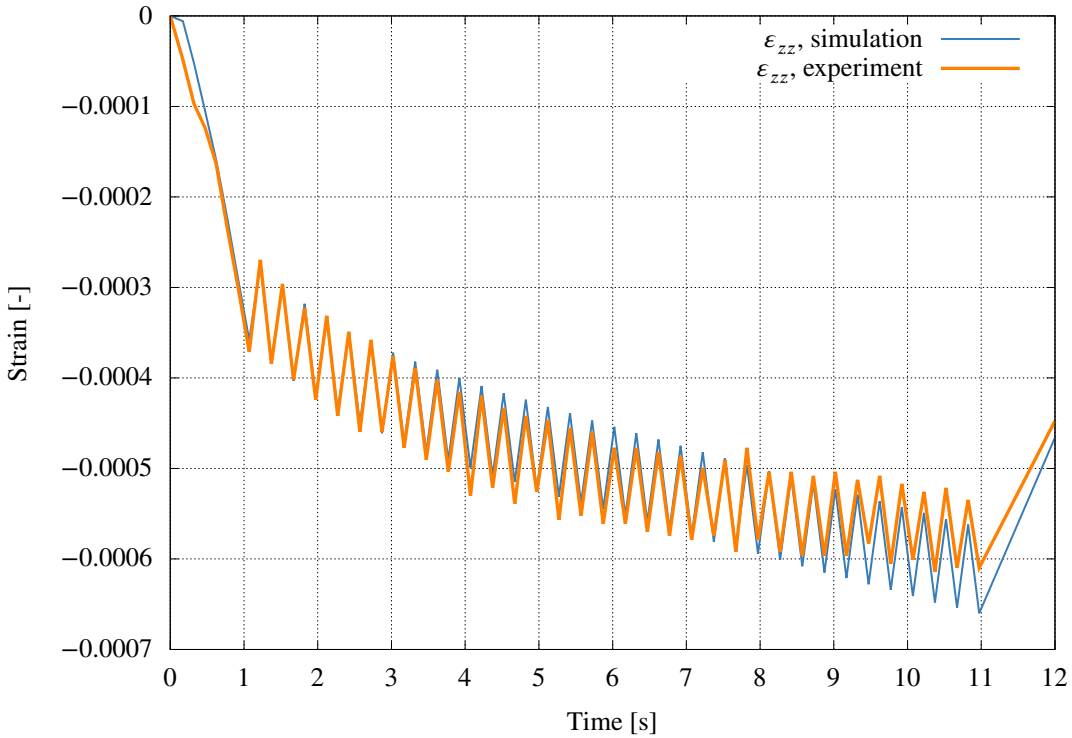

Figure 13 Comparison of the temporal evolution of axial strain during loading.

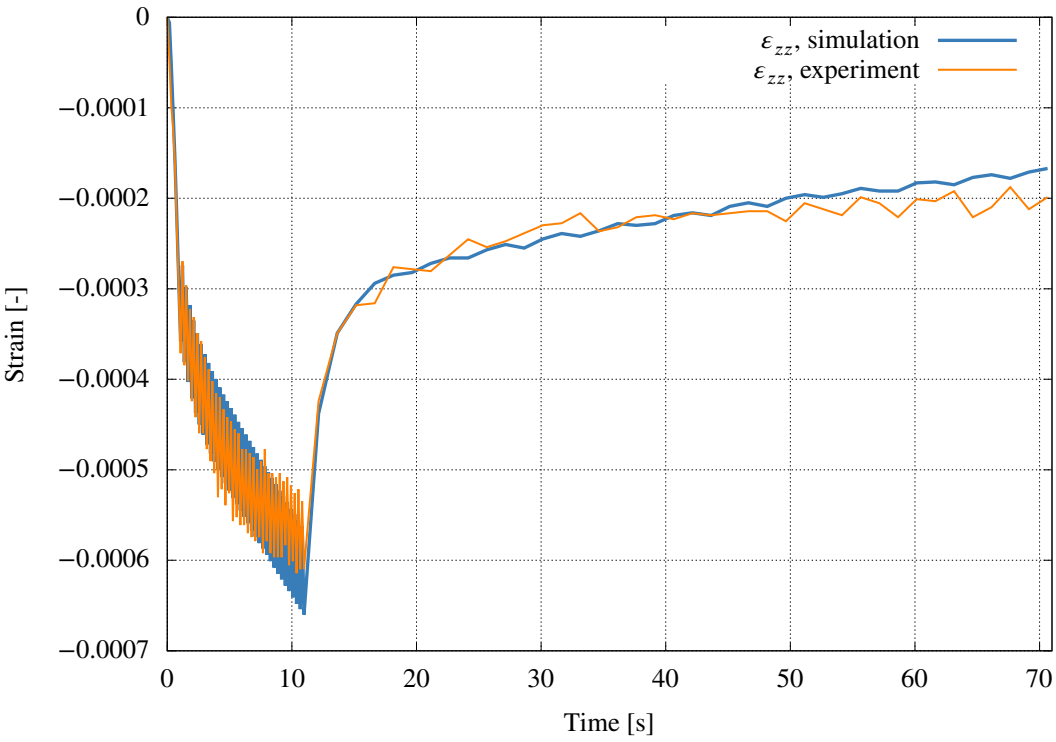

Figure 14 Comparison of the temporal evolution of axial strain over the entire duration of the experiment.

References

1. Zeißler A. *Untersuchungen zum spannungsabhängigen Materialverhalten von Asphalt*. Habilitation thesis, Institut für Stadtbauwesen und Verkehr, Technische Universität Dresden 2015.

2. Wollny I, Hartung F, Kaliske M. Numerical modeling of inelastic structures at loading of steady state rolling. *Computational Mechanics* 2016; 57: 867–886. doi: 10.1007/s00466-016-1266-2

3. Wollny I, Kaliske M. Numerical simulation of pavement structures with inelastic material behaviour under rolling tyres based on an arbitrary Lagrangian Eulerian (ALE) formulation. *Road Materials and Pavement Design* 2012; 14: 71–89. doi: 10.1080/14680629.2012.735800

4. Platen J, Storm J, Bosbach S, Claßen M, Kaliske M. The microlayer model: A novel analytical homogenisation scheme for materials with rigid particles and deformable matrix - applied to simulate concrete. *Computers and Structures* 2024; 293: 107258. doi: 10.1016/j.compstruc.2023.107258

5. Bažant ZP, Oh BH. Microplane Model for Progressive Fracture of Concrete and Rock. *Journal of Engineering Mechanics* 1985; 111: 559-582.

6. Platen J, Zreid I, Kaliske M. A nonlocal microplane approach to model textile reinforced concrete at finite deformations. *International Journal of Solids and Structures* 2023; 267: 112151.

7. Bažant ZP, Kim JJH, Brocca M. Finite strain tube-squash test of concrete at high pressures and shear angles up to 70 degrees. *ACI Materials Journal* 1999; 96: 580–592.

8. Zreid I, Kaliske M. A gradient enhanced plasticity–damage microplane model for concrete. *Computational Mechanics* 2018; 62: 1239–1257.

9. Blanco PJ, Sánchez PJ, Souza Neto dEA, Feijóo RA. Variational foundations and generalized unified theory of RVE-based multiscale models. *Archives of Computational Methods in Engineering* 2016; 23: 191–253.

10. Storm J, Kaliske M. A consistent multi-scale derivation of a micro-plane model within the framework of RVE homogenisation. *Proceedings in Applied Mathematics and Mechanics* 2018; 18: e201800364.

11. Behnke R, Falla GC, Leischner S, Händel T, Wellner F, Kaliske M. A continuum mechanical model for asphalt based on the particle size distribution: Numerical formulation for large deformations and experimental validation. *Mechanics of Materials* 2021; 153: 103703. doi: 10.1016/j.mechmat.2020.103703

12. May M, Wollny I, Platen J, Kaliske M. Microlayer Framework: Extension to Viscoelastic Material Behaviour for Finite Strains. *Proceedings in Applied Mathematics and Mechanics* 2024; 24: e202400165. doi: 10.1002/pamm.202400165

13. Holzapfel AG. *Nonlinear Solid Mechanics*. Chichester: John Wiley & Sons 2000.

14. Fleischhauer R, Behnke R, Kaliske M. A thermomechanical interface element formulation for finite deformations. *Computational Mechanics* 2013; 52: 1039–1058.

15. Fleischhauer R, Thomas T, Kato J, Terada K, Kaliske M. Finite thermo-elastic decoupled two-scale analysis. *International Journal for Numerical Methods in Engineering* 2020; 121: 355–392.

16. Kouznetsova, V.G. . *Computational homogenization for the multi-scale analysis of multi-phase materials*. Mechanics of Materials 2002

17. Hill R. Elastic properties of reinforced solids: Some theoretical principles. *Journal of the Mechanics and Physics of Solids* 1963; 11: 357-372. doi: 10.1016/0022-5096(63)90036-X

18. May M, Konopka D, Storm J, Kaliske M. An anisotropic eigenfracture approach accounting for mixed fracture modes in wooden structures by the Representative Crack Element framework. *Engineering Fracture Mechanics* 2024; 311: 110572. doi: 10.1016/j.engfracmech.2024.110572

19. Bažant ZP. *Microplane Model for Strain-Controlled Inelastic Behavior*: 45–59; New York: John Wiley & Sons . 1984.

20. Platen J, Pauls B, Anantheswar A, Lautenschläger T, Neinhuis C, Kaliske M. A nonlinear finite viscoelastic formulation relative to the viscous intermediate configuration applied to plants. *International Journal for Numerical Methods in Engineering* 2024; 125: e7483.

21. Miehe C. *Zur numerischen Behandlung thermomechanischer Prozesse*. PhD thesis, Institut für Baumechanik und Numerische Mechanik, Universität Hannover 1988.

22. Miehe C. *Kanonische Modelle multiplikativer Elasto-Plastizität: thermodynamische Formulierung und numerische Implementation*. Habilitation thesis, Institut für Baumechanik und Numerische Mechanik, Universität Hannover 1993.

23. Simo J, Miehe C. Associative coupled thermoplasticity at finite strains: Formulation, numerical analysis and implementation. *Computer Methods in Applied Mechanics and Engineering* 1992; 98: 41–104.

24. Shutov A, Ufimtsev K. Approximation-based implicit integration algorithm for the Simo-Miehe model of finite-strain inelasticity. *International Journal for Numerical Methods in Engineering* 2024; 125: e7566. doi: https://doi.org/10.1002/nme.7566

25. Dal H, Kaliske M. Bergström–Boyce model for nonlinear finite rubber viscoelasticity: theoretical aspects and algorithmic treatment for the FE method. *Computational Mechanics* 2009; 44: 809–823.

26. Areias P, Matouš K. Finite element formulation for modeling nonlinear viscoelastic elastomers. *Computer Methods in Applied Mechanics and Engineering* 2008; 197: 4702–4717.

27. Reese S, Govindjee S. Theoretical and numerical aspects in the thermo-viscoelastic material behaviour of rubber-like polymers. *Mechanics of Time-Dependent Materials* 1997; 1: 357–396.

28. Zopf C, Garcia M, Kaliske M. A continuum mechanical approach to model asphalt. *International Journal of Pavement Engineering* 2015; 16: 105–124.

29. Holzapfel GA, Simo JC. A new viscoelastic constitutive model for continuous media at finite thermomechanical changes. *International Journal of Solids and Structures* 1996; 33: 3019–3034.

30. Shutov AV, Landgraf R, Ihlemann J. An explicit solution for implicit time stepping in multiplicative finite strain viscoelasticity. *Computer Methods in Applied Mechanics and Engineering* 2013; 265: 213–225.

31. Landgraf R, Shutov AV, Ihlemann J. Efficient time integration in multiplicative inelasticity. *Proceedings in Applied Mathematics and Mechanics* 2015; 15: 325–326. doi: https://doi.org/10.1002/pamm.201510153

32. Onsager L. Reciprocal Relations in Irreversible Processes. I.. *Physical Review* 1931; 37: 405–426. doi: https://doi.org/10.1103/PhysRev.37.405

33. Weber G, Anand L. Finite deformation constitutive equations and a time integration procedure for isotropic, hyperelastic-viscoplastic solids. *Computer Methods in Applied Mechanics and Engineering* 1990; 79: 173–202.

34. Ma L, Nie W, Zhang X, Yan J, Wang D. Experimental study of Poisson's ratio in indirect tensile test mode for asphalt mixtures. *Construction and Building Materials* 2022; 355: 129288. doi: https://doi.org/10.1016/j.conbuildmat.2022.129288

35. Hansen N, Ostermeier A. Completely Derandomized Self-Adaptation in Evolution Strategies. *Evolutionary Computation* 2001; 9: 159–195. doi: 10.1162/106365601750190398

36. Blank J, Deb K. pymoo: Multi-Objective Optimization in Python. *IEEE Access* 2020; 8: 89497-89509.